Optical and near-UV spectroscopic properties of low-redshift jetted quasars in the main sequence context

Shimeles Terefe Mengistue [1,2,3★†], Ascensión Del Olmo [4★], Paola Marziani,[5★] Mirjana Pović,[1,4,6] María Angeles Martínez-Carballo,[7] Jaime Perea[4] and Isabel Márquez [4]

[1]*Space Science and Geospatial Institute (SSGI), Entoto Observatory and Research Centre (EORC), Astronomy and Astrophysics Research and Development Division, P.O. Box 33679, Addis Ababa, Ethiopia*
[2]*Addis Ababa University (AAU), P.O. Box 1176, Addis Ababa, Ethiopia*
[3]*Jimma University, College of Natural Sciences, Department of Physics, P.O. Box 378, Jimma, Ethiopia*
[4]*Instituto de Astrofísica de Andalucía (IAA-CSIC), Glorieta de la Astronomia s/n, Granada E-18008, Spain*
[5]*Istituto Nazionale di Astrofisica (INAF), Osservatorio Astronomico di Padova,vicolo dell' Osservatorio 5, Padova I-35122, Italy*
[6]*Physics Department, Faculty of Science, Mbarara University of Science and Technology (MUST), P.O. Box 1410, Mbarara, Uganda*
[7]*Department of Applied Mathematics and IUMA, Computational Dynamics group, University of Zaragoza, E-50009, Zaragoza, Spain*

Accepted 2023 August 10. Received 2023 August 6; in original form 2022 October 12

ABSTRACT

This paper presents new optical and near-UV spectra of 11 extremely powerful jetted quasars, with radio to optical flux density ratio $>10^3$, which concomitantly cover the low-ionization emission of MgIIλ2800 and Hβ as well as the FeII blends in the redshift range $0.35 \lesssim z \lesssim 1$. We aim to quantify broad emission line differences between radio-loud (RL) and radio-quiet (RQ) quasars by using the 4D eigenvector 1 parameter space and its main sequence (MS) and to check the effect of powerful radio ejection on the low-ionization broad emission lines. The Hβ and MgIIλ2800 emission lines were measured by using non-linear multicomponent fittings as well as by analysing their full profile. We found that broad emission lines show large redward asymmetry both in Hβ and MgIIλ2800. The location of our RL sources in a UV plane looks similar to the optical one, with weak $\mathrm{FeII_{UV}}$ emission and broad MgIIλ2800. We supplement the 11 sources with large samples from previous work to gain some general inferences. We found that, compared to RQ, our extreme RL quasars show larger median Hβ full width at half maximum (FWHM), weaker FeII emission, larger M_{BH}, lower $L_{\mathrm{bol}}/L_{\mathrm{Edd}}$, and a restricted bf space occupation in the optical and UV MS planes. The differences are more elusive when the comparison is carried out by restricting the RQ population to the region of the MS occupied by RL sources, albeit an unbiased comparison matching M_{BH} and $L_{\mathrm{bol}}/L_{\mathrm{Edd}}$ suggests that the most powerful RL quasars show the highest redward asymmetries in Hβ.

Key words: line: profiles – galaxies: active – quasars: emission lines – quasars: general – quasars: supermassive black holes.

1 INTRODUCTION

Type I active galactic nuclei (AGNs) exhibit distinct features that are not seen in normal galaxies, such as a power-law continuum shape in ultraviolet (UV) and optical bands with a number of broad and narrow emission lines emitted by ionic species over a wide range of ionization potentials (e.g. Osterbrock & Mathews 1986; Vanden Berk et al. 2001; Netzer 2015). They show widely different properties among themselves (Osterbrock & Pogge 1985; Boroson & Green 1992; Strateva et al. 2003; Ho 2008; Śniegowska et al. 2018): different line profiles, intensity ratios, and ionization levels (e.g. Gaskell 1982; Corbin 1997; Sulentic et al. 2007; Marziani et al. 2010). Since the discovery of quasi-stellar radio sources and quasistellar objects (quasars).[1] In the early 1960s, there is a general consensus about their nature: they are thought to be powered by matter accreting on to a supermassive black hole (SMBH) capable of producing emission across the majority of the electromagnetic spectrum. They are among the most powerful, distant, and luminous objects in the Universe reaching luminosities $\gtrsim 10^{48}$ ergs s^{-1} (e.g. Rees 1984; Peterson 1997; Bañados et al. 2018) although much of the empirical understanding is still to be developed. The last three decades have opened promising lines of investigation on the definition and contextualization of optical and UV properties (e.g. Boroson & Green 1992; Sulentic, Marziani & Dultzin-Hacyan 2000a; Shen & Ho 2014; Wolf et al. 2020), with the exploration of a spectroscopic unification for broad-line emitting AGN, like the four-dimensional eigenvector 1 (4DE1) parameter space that organizes quasar diversity (Sulentic et al. 2000b).

Type 1 AGN have been classified into two distinct classes using the ratio of their radio to optical flux densities (Kellermann et al. 1989), which are thought to correlate with the presence or absence of extended relativistic radio jets. These are known as radio-loud (RL) and radio-quiet (RQ), respectively (e.g. Antonucci 1993; Urry & Padovani 1995; Blandford, Meier & Readhead 2019).

★ E-mail: shimeles11@gmail.com (STM); chony@iaa.es (ADO); marziani@inaf.it (PM)
† Visiting researcher at the IAA-CSIC as a PhD fellow.

[1]In the following, we will use the quasar as an umbrella term that includes all type-1 AGN regardless of luminosity and radio power.

With the improvement of radio interferometry techniques, it was possible to notice that both classes are capable of producing radio jets, although RQ jets are far less powerful and at least in some cases sub-relativistic (e.g. Ulvestad et al. 1998; Blundell, Beasley & Bicknell 2003; Middelberg et al. 2004; Ulvestad, Antonucci & Barvainis 2005; Gallimore et al. 2006; Hartley et al. 2019; Sbarrato et al. 2021). The radio power of RQ quasars can be even 2–3 orders of magnitude lower than that of their RL counterparts for the same optical power. Padovani et al. (2017) argues that the classification should be based on a fundamentally physical rather than just an observational difference, namely the presence (or lack) of strong relativistic jets and that we should use the term 'jetted' and 'non-jetted'. From the theoretical point of view, in spite of the great advancement in the ability to collect sets of data with very long baseline interferometry (VLBI), the formation of the relativistic radio jet in quasars is still an open question (see e.g. Urry & Padovani 1995; Blandford et al. 2019; Davis & Tchekhovskoy 2020, and references therein).

In this paper, we will be concerned with debated problems associated with the possibility of a real physical dichotomy between RL and RQ quasars (e.g. Xu, Livio & Baum 1999; Cirasuolo et al. 2003; Zamfir, Sulentic & Marziani 2008; Coziol et al. 2017; Blandford et al. 2019; Panessa et al. 2019): the effect of radio loudness on the dynamics of the low-ionization broad-line emitting regions.

The singly ionized iron emission is systematically fainter in RL than in RQ sources, although it is still unclear if this is an effect intrinsic to a different emitting region structure, or associated with different host-galaxy properties (e.g. Marziani et al. 2021, and references therein).

To this aim, we utilize a parameter space that provides spectroscopic contextualization for all classes of broad-line emitting AGN, the 4DE1 concept (e.g. Sulentic et al. 2000b). The four dimensions of the space are:

(i) Full width at half maximum (FWHM) of Hβ full broad profile (H$\beta_{\rm FP}$; see Section 3.2) related to the velocity field of the low-ionization line (LIL)-emitting region;

(ii) Intensity ratio of the optical FeIIλ4570Å (which is the sum over 4434–4684Å) and H$\beta_{\rm FP}$, $R_{\rm FeII,\,opt}$ = I(FeIIλ4570Å)/I(H$\beta_{\rm FP}$). $R_{\rm FeII}$ is affected by physical conditions such as density, ionization level, and metal content (Panda, Marziani & Czerny 2019b).

(iii) Centroid shift at half maximum of the CIVλ1549Å, that measures the prominence of an outflowing/wind component (e.g. Richards et al. 2011), and

(iv) Soft X-ray photon index ($\Gamma_{\rm soft}$) that depends on the accretion state (see e.g. Sulentic et al. 2000b; Jin, Done & Ward 2017; Panda et al. 2019a).

The two first parameters define the optical plane of the 4DE1 parameter space, the quasar main sequence (hereafter MS, Marziani et al. 2001; Sulentic et al. 2002; Marziani et al. 2010; Shen & Ho 2014; Wolf et al. 2020). The main advantage of the 4DE1 parameter space formulation is its weak dependence on source luminosity (e.g. Zamfir et al. 2008).

This formalism also assisted the interpretation of several observational aspects that appear puzzling if, for example, sets of spectra are indiscriminately averaged together. Spectra can be averaged, but only in a well-defined context like the 4DE1 (Sulentic, Marziani & D'Onofrio 2012). In addition, it helps to establish a connection between an observational set of accretion parameters such as black hole mass ($M_{\rm BH}$) and Eddington ratio ($\lambda_{\rm E} = L_{\rm bol}/L_{\rm Edd}$; see e.g. Fraix-Burnet et al. 2017; Marziani et al. 2018, and references therein).

Exploration of the 4DE1 parameter space gave rise to the concept of two populations of quasars that present important spectroscopic differences (Sulentic et al. 2007):

(i) Population A (hereafter Pop. A), whose sources generally have H$\beta_{\rm FP}$ FWHM $< 4000\,{\rm km\,s^{-1}}$, show Lorentzian profiles in the broad emission lines, tend to have $R_{\rm FeII,\,opt} > 0.5$, significant blueshifts in high-ionization lines (HILs; e.g. CIVλ1549) and soft X-ray excess.

(ii) Population B (hereafter Pop. B), with a very wide range of H$\beta_{\rm FP}$ FWHM, with values higher than $4000\,{\rm km\,s^{-1}}$, show Gaussian profiles (a broad and an additional very broad redshifted component), $R_{\rm FeII,\,opt} < 0.5$. In general, at low-z, they do not show significant blueshifts in HILs and no soft X-ray excess.

The physical distinction between the two populations is related to the fact that Pop. A are fast-accreting objects with a relatively small $M_{\rm BH}$; meanwhile, Pop. B are the ones with high $M_{\rm BH}$ and low Eddington ratios (Marziani et al. 2009). At low $z(\lesssim 1)$, most powerful RL sources belong to Pop. B (Sikora, Stawarz & Lasota 2007; Zamfir et al. 2008).

As suggested in Zamfir et al. (2008), the value of studying the RL phenomenon within the 4DE1 context is at least twofold: (i) the approach compares RL and RQ quasars in a parameter space defined by measures with no obvious dependence on the radio properties (Sulentic et al. 2003); and (ii) it allows predictions of the probability of radio loudness for any AGN population given a specific set of spectroscopic properties. Open questions are whether the geometry/kinematics of RQ and RL quasars is the same or not. A related issue is also the ability to distinguish between high and low accretors from optical and UV spectroscopy, to assess any effect the black hole spin has, and to infer the structure of the accretion disc (e.g. Sikora et al. 2007; Lagos, Padilla & Cora 2009; Tchekhovskoy, McKinney & Narayan 2009).

This work presents new optical and near-UV spectra and a multicomponent fitting analysis of 11 jetted Pop. B (RL) quasars at low–z ($0.3 \lesssim z \lesssim 1$). This paper extends the study to near-UV with the coverage of the MgIIλ2800Å (hereafter MgII) spectral range, providing still rare simultaneous observations of Hβ and MgII. Both Hβ and MgII provide diagnostics of the LIL part of the emitting region. In addition, MgII is known to be less affected by shifts and asymmetries than Hβ and is expected to provide a reliable virial black hole mass estimation (e.g. Trakhtenbrot & Netzer 2012). The sources we selected are among the most extreme radio emitters, those with a radio to optical flux density ratio $\gtrsim 10^3$. For them, we want to test if there might be a strong effect of the relativistic jets on the low-ionization UV and optical lines emission. Section 2 describes the new AGN sample, the main comparison samples, the new observations from the 3.5 m telescope at the Calar Alto Observatory (CAHA), and the archival radio data.

Spectral non-linear multicomponent fittings and FP analysis are described in Section 3. The results of spectral fittings and observed trends are described in Section 4.

We discuss the results in Section 5 and conclude in Section 6. Throughout this paper, we adopt a flat ΛCDM cosmology with $\Omega_\Lambda = 0.7$, $\Omega_0 = 0.3$, and $H_0 = 70\,{\rm km\,s^{-1}\,Mpc^{-1}}$.

2 SAMPLE AND DATA

2.1 Sample selection

Table 1 presents the main properties of our sample, reporting the quasar identification (Column 1), the equatorial coordinates at J2000 (Columns 2 and 3), the median redshift estimated for each quasar

Table 1. Summary of sample properties, and observations with CassegrainTWIN spectrograph of the 3.5 m telescope at the Calar Alto Observatory.

Object	Coordinates		z	m^a	M_B^a	Date of observation	Total exp. time (s)	Airmass	S/N
	RA (2000)	Dec. (2000)							
(1)	(2)	(3)	(4)	(5)	(6)	(7)	(8)	(9)	(10)
PHL 923	00 59 05.6	+ 00 06 51	0.7183	17.9	−24.6	22-10-2012	3600	1.26	18
B2 0110 + 29	01 13 24.2	+ 29 58 16	0.3625	17.0	−24.2	23-10-2012	2700	1.08	12
3C 37	01 18 18.5	+ 02 58 06	0.6667	18.8	−23.7	23-10-2012	3600	1.29	20
PKS 0230–051	02 33 22.1	−04 55 08	0.7807	17.0	−25.9	23-10-2012	3600	1.47	43
3C 94	03 52 30.6	−07 11 02	0.9648	16.7	−26.4	23-10-2012	2700	1.48	34
PKS 0420–01	04 23 15.8	−01 20 33	0.9136	17.0	−25.9	22-10-2012	3600	1.30	38
3C 179	07 28 10.8	+ 67 48 47	0.8416	18.4	−24.9	23-10-2012	3600	1.17	19
3C 380	18 29 31.8	+ 48 44 46	0.6919	16.8	−25.5	23-10-2012	2700	1.12	40
S5 1856 + 73	18 54 57.4	+ 73 51 19	0.4604	16.8	−25.0	23-10-2012	3600	1.35	68
PKS 2208–137	22 11 24.1	−13 28 10	0.3912	17.0	−24.4	23-10-2012	2700	1.62	18
PKS 2344 + 09	23 46 37.0	+ 09 30 45	0.6724	15.9	−26.3	22-10-2012	3600	1.16	74

Column 2 is in units of hours, minutes, and seconds. Column 3 is in units of degrees, minutes, and seconds. [(a)] From the catalogue of quasars and AGNs (Véron-Cetty & Véron 2010, 13th Edn.), Column 5 corresponds to the apparent magnitude, and Column 6 is the absolute magnitude in the B-band.

as explained in Section 2.2.1 (Column 4), the apparent and absolute magnitudes taken from Véron-Cetty & Véron (2010) (Columns 5 and 6, respectively) from where we also took the initial redshift for the sample selection, and a summary of the observations (see Section 2.2). We selected 11 RL quasars based on their strong radio emission that satisfies a criterion of extreme radio loudness, with values of the Kellermann parameter (Kellermann et al. 1989, radio to optical flux density ratio) R_K exceeding 10^3 (see Sections 2.3 and Table 3, Columns 6 and 7). Such extremely powerful jetted sources permit a detailed study of the effects of powerful radio ejections on the low-ionization broad-line region (BLR). The 11 sources are optically bright, with $\log L_{Bol}$ in the range of 44.9–46.7 [ergs s^{-1}], and were selected in a redshift range ($0.35 \lesssim z \lesssim 1$; Véron-Cetty & Véron 2010) that makes possible the concomitant coverage of Hβ and MgII. Such observations provide consistent information, as observed spectra at different times may suffer a significant continuum variability. Our high signal-to-noise spectra with spectral range 3500–10 000 Å provide an extended view of the quasar continuum in each spectral region and allows us to make accurate measurements of emission line parameters such as the intensity of optical and UV FeII features.

There are not so many RL AGN with radio loudness parameter, $R_K \gtrsim 10^3$ (see Section 2.3), and the uniqueness of this study rests on the selection of extremely powerful jetted sources. In our sample, all sources are not only with $\log R_K \gtrsim 3$, but 6 of them are with $\log R_K \gtrsim 4$ (see the histogram in Fig. 1 in which we showed the distribution of the radio loudness parameter that was estimated by using the 1.4 GHz radio flux density and the g-band optical flux density in all the cases). Only a handful of sources in the main comparison samples (see below) have $R_K \gtrsim 10^4$ and a few tens have $\gtrsim 10^3$.

In the optical plane of 4DE1 parameter space, our extreme $\log R_K \gtrsim 3$ (hereafter eRk) represent non-negligible addition to RL sub-samples of optically selected quasars that are represented in Population B STs (Zamfir et al. 2008). The eRk sample enhances the significance of statistical comparisons between the highest radio loudness sources and RQ as well as other RL sub-samples.

2.1.1 *Main comparison samples*

As main comparison samples in the optical, we used the low redshift samples of Marziani et al. (2003a) and Zamfir et al. (2010). The

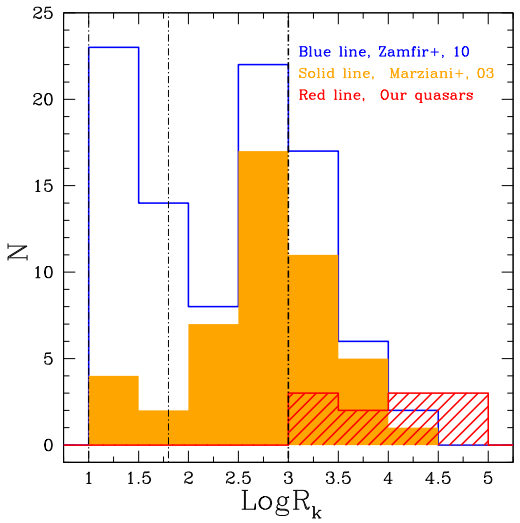

Figure 1. Distribution of radio loudness parameter for Pop. B RLs from our sample (red striped area) and the main comparison samples used in this work, Marziani et al. (2003a; solid orange) and Zamfir et al. (2010; blue line). The vertical dot–dashed lines at 1 and 1.8 mark the nominal RQ-RI and RI-RL boundaries (Ganci et al. 2019). The vertical dot–dashed line at 3 marks the boundary for extreme radio loudness values.

redshift and luminosity ranges, the number of sources (both Pop. A and B) considered in each sample, the number of Pop. B RL sources in different radio loudness ranges, as well as the emission lines used and profile measures available in each one are summarized in Table 2. The sample of Zamfir et al. (2010) consists of 469 quasars of which 209 are classified as Pop. B.

The sample of Marziani et al. (2003a) originally has 215 sources. Before using it as a main comparison sample, we excluded sources in common with the other comparison sample (38) and also nine sources that may create doubt in the interpretation of the spectra, due mainly to a noisy spectrum, the presence of a strong stellar continuum or strong star formation, after a careful examination. The 168 remaining objects, of which 94 belong to Pop. B, contain information for the line centre [c($\frac{1}{2}$)] and the line base [c($\frac{1}{4}$)] of Hβ. These measurements provide an empirical description of the full line profile, i.e. velocity

Table 2. Summary of main comparison samples and this work (eRk) sample.

Information	Marziani + 03	Zamfir + 10	Marziani + 13[a]	This work[b]
Redshift range	z < 0.8	z < 0.7	0.4 < z < 0.75	0.35 < z < 1
No. of sources	168	469	8[a]	11
Parameters	c($\frac{1}{2}$), c($\frac{1}{4}$), R_K FWHM,AI	c($\frac{1}{4}$), R_K, AI FWHM,$R_{FeII,\ opt}$	c($\frac{1}{2}$), c($\frac{1}{4}$) FWHM,AI	c($\frac{1}{2}$), c($\frac{1}{4}$), R_K FWHM, AI $R_{FeII,\ opt}$,$R_{FeII,\ UV}$[b]
Lines used	Hβ	Hβ	Hβ and MgII	Hβ and MgII
Log L_{bol} (ergs s^{-1})	43.7–47.8	43.0–47.0	45.7–46.9	45.15–46.57
No. Pop. B RLs:				
logR_K>1.8	42	61	–	11
logR_K>3	17	25	–	11
logR_K>4	1	2	–	6

[a]This sample provides eight composite spectra generated by using spectral binning of physically similar quasars of 680 SDSS spectra. [b]All the profile parameters measured for our eRk quasars, both in the FP and the multicomponent fittings, are detailed in the following sections. c($\frac{1}{2}$) and c($\frac{1}{4}$) represent the centroid velocity shift at $\frac{1}{2}$ and $\frac{1}{4}$ fractional intensity of the line, respectively. AI denotes the asymmetry index.

Table 3. Radio properties of the sample.

Object	NVSS Int. flux (mJy)	FIRST Int. flux (mJy)	Flux at 5 GHz[(a)] (mJy)	$\alpha^{(b)}$	$log\,R_K^{(c)}$	$log\,R_{KS}^{(d)}$	$log(P_\nu)$	Morph.
(1)	(2)	(3)	(4)	(5)	(6)	(7)	(8)	(9)
PHL 923	2508 ± 75	2494	1410	0.42	4.63	4.37	34.63	CL
B2 0110 + 29	810 ± 9	–	311	0.54	4.34	3.99	33.50	LD
3C 37	1522 ± 46	1646	621	0.92	4.49	4.15	34.45	CL
PKS 0230–051	210 ± 8	139	160	0.52	3.13	3.03	33.59	CL
3C 94	3061 ± 112	2798	790	1.04	4.23	3.57	35.18	LD
PKS 0420–01	2726 ± 82	–	1580	0.23	3.94	3.71	34.71	LD
3C 179	2123 ± 75	–	1000	0.72	4.63	4.29	34.79	CL
3C 380	13753 ± 413	–	5000	0.75	4.73	4.34	35.41	CL
S5 1856 + 73	490 ± 16	–	610	0.12	3.03	3.22	33.42	C
PKS 2208–137	1330 ± 40	–	620	0.66	3.71	3.45	33.81	CL
PKS 2344 + 09	1804 ± 54	1734	1690	0.19	3.44	3.49	34.37	C

[(a)] From (Véron-Cetty & Véron 2010). [(b)] From Vollmer et al. (2010). [(c)] With NVSS k-corrected radio flux density at 1.4 GHz and optical rest-frame flux density in g band. [(d)] With k-corrected radio flux density at 5 GHz and rest-frame optical flux density in B band. Units in Column 8 are ergs s^{-1}Hz^{-1}.

shifts at different fractional intensities of the FP, e.g. at the line base, at the line centre, and at peak fractional intensities [c($\frac{9}{10}$)].

We also use in particular for the MgII region the composite spectra from Marziani et al. (2013) built for different spectral types (STs) along the MS, i.e. A1 to A4 for Pop. A quasars and in Pop. B for the STs B1, B2, B1$^+$, and B1^{++} as well as within the B1 bin for those classified by the authors as RL. The composite spectra from that sample have a measurement for both UV and optical regions.

Other secondary samples used in specific points such as those of Wang et al. (2009) and the QSFIT catalogue (Calderone et al. 2017) are described in the corresponding sections (Sections 4.3 and 4.4).

2.2 Optical and UV observations

Long-slit optical observations were obtained with the Cassegrain TWIN spectrograph of the 3.5 m telescope at the CAHA (Almería, Spain)[2] The TWIN spectrograph is optimized to cover a wavelength range from about 3400 to 10 000 Å, dividing the light from the slit in two channels (blue and red) by a dichroic mirror. We selected the beam splitter at 5500 Å and gratings T13 and T11, for the blue and the red channels, respectively, in order to obtain simultaneously the spectra corresponding to the MgII and Hβ regions at the redshift of the objects of our sample. T13 grating provides a spectral coverage from 3500 to 5500 Å with a reciprocal dispersion of 2.14 Å pixel^{-1}, meanwhile, T11 grating covers the range from 5400 to 10 000 Å with a spectral dispersion of 2.41 Å pixel^{-1}.

Table 1 with the main properties of the sample also summarizes the observations where is listed the date of observation (Column 7), the total exposure time in seconds (Column 8), the air mass (Column 9), and the signal-to-noise ratio (S/N) measured in the continuum (Column 10). The observations were obtained with a slit width of 1.2 arcsec and oriented at the paralactic angle in order to minimize the effects of atmospheric differential refraction in the spectra. The total exposure time required for each object was split into three exposures to reduce the number of cosmic rays and eliminate them by combining different exposures.

Data reduction were carried out in a standard way using IRAF[3] (Tody 1986). Spectra were bias and overscan corrected and flat-fielded with a normalized flat-field obtained from a median combi-

[2]http://www.caha.es/

[3]IRAF is the Image Reduction and Analysis Facility, a general purpose software system for the reduction and analysis of astronomical data, iraf.net

nation of the flats obtained for each spectral region (blue and red). Wavelength calibration was obtained using the standard lamps (He-Ar and Fe-Ne) exposures and standard IRAF tasks. The apall task in IRAF was used for object extraction and background subtraction. Instrumental response and absolute flux calibration were obtained each night through observations done with the same instrumental setup of two spectrophotometric standard stars, G191B2B and BD + 28d4211. They were also used to remove telluric bands that are mainly observed in the red channel. The final calibrated rest-frame spectra of all the sources, once the blue (MgII region) and red (Hβ region) spectra were combined for each object, are shown in Fig. 1.

2.2.1 *Redshift determination*

We determine the redshift of the quasars, following Bon et al. (2020), by measuring the observed vacuum wavelengths of individual narrow emission lines, in particular [OII]λ3727Å, Hδ, Hγ, Hβ, and [OIII]$\lambda\lambda$4959,5007ÅÅ that are available in our spectra. For that, we used the IRAF task splot, and by taking mainly as reference vacuum wavelengths the ones from Vanden Berk et al. (2001). The median value of the redshift obtained from the different narrow emission lines was adopted as the empirical redshift of each object (reported in Table 1, Column 4) and then used for getting the rest-frame spectrum of each quasar. Typical rms in the estimated redshifts are between 0.0003 and 0.001.

2.3 Archival radio data

Table 3 presents the main radio properties of the sample. The radio fluxes were obtained at 1.4 GHz (20 cm) from the National Radio Astronomy Observatory Very Large Array (VLA) Sky Survey (NVSS[4]; Condon et al. 1998) and at 5 GHz (6 cm) from Véron-Cetty & Véron (2010)[5] catalogue. We also list in Column 3 the integrated flux at 1.4 GHz compiled from the Faint Images of the Radio Sky at Twenty centimetres (FIRST)[6] survey (Becker, White & Helfand 1995) for the only five sources of our sample observed by FIRST.

As we mentioned in the introduction, quasars have been classified as RL and RQ by using radio and optical measurements as well. However, a clear consensus on a boundary between RL and RQ quasars has been difficult to achieve and several radio-loudness criteria have been used in the literature (see e.g. White, Becker & Helfand 2005; Hao et al. 2014; Kellermann et al. 2016; Chakraborty et al. 2022, and references therein). One of the most commonly used criteria is the radio-loudness parameter defined by Kellermann et al. (1989), $R_{\rm KS}$, as the ratio of the radio flux density at 5 GHz to the B-band optical flux density. In this work, we have used a modified version of the radio-loudness parameter, currently commonly used, based on the ratio of the rest-frame radio flux density at 1.4 GHz to the rest-frame optical flux density in the g-band, $R_{\rm K}$ (e.g. Zamfir et al. 2008; Gürkan et al. 2015). For completeness, we also estimated the Kellermann parameter in rest-frame units ($R_{\rm KS}$).

To estimate the radio-loudness parameters, the k-corrected radio flux density at 1.4 and 5 GHz was found from the observed radio flux densities (reported in Table 3, Columns 2 and 4, respectively) by using the spectral index α obtained from Vollmer et al. (2010; reported in Table 3, Column 5) and the relation from Ganci et al. (2019)

$$f_{\nu_{o,e}} = f_{\nu,o}\left[(1+z)^{\alpha-1}\right] \quad (1)$$

where the subscript *'o'* refers to the observer's frame, and the subscript *'e'* refers to quantities in the quasar rest frame. In all the calculations, we used the convention for the spectral index, $S \propto \nu^{-\alpha}$. We have FIRST radio data only for five of our sources (see Table 3, Column 3), and hence we used the NVSS 1.4 GHz fluxes.

The rest-frame optical fluxes around the effective wavelengths λ 4770Å (for g band) and λ 4450Å (for B band) were obtained from our rest-frame spectra. The resulting radio loudness parameters are reported in Columns 6 and 7 of Table 3, respectively. Throughout this paper, we used the modified radio loudness parameter ($R_{\rm K}$). Also, radio power (P_ν) has been calculated by using Shankar, Dai & Sivakoff (2008, their equation 1) and is reported in Column 8. Previous works showed a well-defined lower limit for $R_{\rm K}$ in which lobe dominated (LD) RL sources have a value of $\log R_{\rm K} > 1.8$ and a radio power $\log P_\nu > 31.6$ (ergs s^{-1} Hz^{-1}; e.g. Sulentic et al. 2003; Zamfir et al. 2008). Ganci et al. (2019) also classified sources on the basis of $R_{\rm K}$, as radio detected (RD; sources with $\log R_{\rm K} < 1.0$), radio intermediate (RI; $1.0 \leq \log R_{\rm K} < 1.8$) and RL ($\log R_{\rm K} \geq 1.8$). According to these classifications, all our sources are strong radio emitters and can be labelled as strong RLs. As can be seen in Table 3, the resulting radio-power for all our quasars is also extremely high with $\log P_\nu$ between 33.5 and 35.4 [ergs s^{-1} Hz^{-1}] and with $\log R_{\rm K} > 3$, by far meeting the requirement to classify them as RL.

2.3.1 *Radio morphology classification*

A morphological radio classification of our sample at an angular scale of arcsec was obtained with the NVSS images and supplemented by FIRST images for the five objects also observed in that survey. This is the scale related to a kpc-sized scale associated with extended features such as the radio lobes and normally used in the majority of the comparison samples. We classified our sources according to the following scheme: as core dominated (C) if the core appears unresolved; as core plus lobe/s (CL), if we have a visible bright core and at least one lobe, and as lobe-dominated (LD), if we see the lobes without core in the spatial scales of VLA or if the radio emission is dominated by lobes. This classification for our quasars is provided in Column 9 of Table. 3. In this scale, we have 2, 6, and 3 quasars with C, CL, and LD radio morphology, respectively. Also, our quasars present inner jets at parsec and sub-parsec scales (milli-arcsecs scale, VLBA/I), as expected for strong radio emitters. Plavin, Kovalev & Pushkarev (2022) provides information on the estimated distance between the VLBI core and a structure assigned to a jet/s for 8/11 of our sources.

In this paper, we used the kpc scale, which is available for the whole sample and is the most widely used in literature and in the comparison samples. In appendix A of the online supplemental material, we included the FIRST images and their overlay on the optical Pan-STARRS image for PHL 923, 3C 37, PKS 0230–051, 3C 94, and PKS 2344+09. In addition, for two sources (B2 0110 + 29 and PKS 2208–137) that do not have the FIRST cut-out image, we present NVSS radio maps, that we used for the morphological classification.

3 SPECTRAL ANALYSIS

Narrow and broad emission lines are prominent features in optical and UV spectra of type I AGN (Osterbrock 1988). In this work, the analysis of each spectrum was performed independently in the two observed spectral regions, corresponding to the blue and red arms of the spectrograph, respectively. The red arm includes both low-ionization features such as Hβ, FeIIλ4570Å, and HILs like [OIII]$\lambda\lambda$4959,5007ÅÅ (hereafter [O III]) as main representatives.

[4]NVSS-https://www.cv.nrao.edu/nvss/NVSSPoint.shtml
[5]https://vizier.u-strasbg.fr/viz-bin/VizieR-3?-source = VII/258/vv10
[6]FIRST-http://sundog.stsci.edu/cgi-bin/searchfirst

The low-ionization MgII doublet is located in the redshifted UV region along with prominent $\mathrm{FeII_{UV}}$ emission covered by the blue arm. In each region, we carried out a multicomponent non-linear fitting and an analysis of the FP of the emission lines, as it is described in the next subsections.

3.1 Spectral fitting

3.1.1 Optical region

In order to get relevant physical parameters for the emission lines observed in our spectra, an empirical model that matches the observed spectrum was applied. Our spectral non-linear multicomponent fitting was carried out by using `IRAF specfit` routine, which can fit data spanning a large range in wavelength by using a non-linear χ^2 minimization technique (Kriss 1994), and used in previous studies (e.g. Marziani et al. 2010; Martínez-Aldama et al. 2015; Sulentic et al. 2017). This allowed us to simultaneously fit a continuum, a scalable FeII emission, and individual emission lines yielding FWHM, peak wavelengths, and intensities of all emission line components. To get the best fit, we first used a simplex algorithm with an iteration up to 200 and afterward, a Levenberg–Marquardt algorithm with a lower number of iterations to ensure convergence to the global minimum χ^2 (Levenberg 1944).

For non-linear multicomponent fitting, we included the following components and conditions in the fittings:

(i) A power law local continuum underlying the Hβ region to take into consideration the thermal accretion disc emission in optical (Shields 1978). We defined the continuum by using three to four regions that are free of emission lines.

(ii) A scalable FeII template for modelling the $\mathrm{FeII_{opt}}$ emission lines that are blended with Hβ, as FeII has a large number of transitions producing overlapping and blended lines (Marziani et al. 2009).

(iii) We assumed that the Balmer line Hβ has three components with Gaussian profiles, as appropriate for Pop. B sources (e.g. Buttiglione et al. 2010; Marziani et al. 2010):

a) A narrow component (NC) that represents the narrow-line region (NLR) with low-density and more slowly moving clouds with narrow-line width, which infers this region is far from the central SMBH;

b) A broad component (BC) associated with the BLR with almost unshifted component and corresponds to dense and fast-moving clouds that indicates the proximity to the central SMBH;

c) A very broad component (VBC) associated with a very broad-line region (VBLR) with high-ionization and large column density that corresponds to broader and redshifted components.

(iv) The [O III] emission lines, represented by two Gaussian NC set at rest-frame plus two blueshifted semi-broad components (SBCs).

(v) A HeIIλ4686Å line when there were hints of its presence with a BC and/or VBC component.

The fitting for this region was done in a different wavelength range (see Table 4 Column 2) for each object to account for the complex nature observed in some of the spectra, like PHL 923 and 3C 94. In the fitting procedure, the number of free parameters was reduced by assuming constraints related to emission lines coming from the same region. All the narrow lines were assumed to have roughly the same width and shift. The two [O III] lines were assumed to have a flux

Table 4. Results of the FP and the `specfit` analysis for Hβ.

			Full broad profile (FP) (BC + VBC)									NC			BC				VBC			
Object	$f_{\lambda,5100}$	Fitting range	EW	I	FWHM	C($\frac{1}{4}$)	C($\frac{1}{2}$)	C($\frac{3}{4}$)	C($\frac{9}{10}$)	AI	KI	FeIIλ4570 SF	$R_{\mathrm{FeII,opt}}$	I	Shift	FWHM	I	Shift	FWHM	I	Shift	FWHM
(1)	(2)	(3)	(4)	(5)	(6)	(7)	(8)	(9)	(10)	(11)	(12)	(13)	(14)	(15)	(16)	(17)	(18)	(19)	(20)	(21)	(22)	(23)	(24)
PHL 923	0.13	4400–5100	92	13.2	4420 ± 80	2280 ± 880	−60 ± 140	−190 ± 120	230 ± 160	0.47 ± 0.11	0.25 ± 0.05	8.40	2700	0.63	0.4	10	810	5.8	−330	3640	7.4	4370	11 400
B2 0110 + 29	0.07	4400–5200	138	9.4	6370 ± 740	1690 ± 540	450 ± 250	130 ± 170	60 ± 210	0.28 ± 0.08	0.31 ± 0.04	0.01	4000	0.001	0.6	−40	510	3.4	−1	4650	6.0	2030	12 000
3C 37	0.13	4400–5200	126	17.7	5540 ± 450	550 ± 300	490 ± 160	470 ± 150	470 ± 200	0.02 ± 0.13	0.41 ± 0.05	2.8	2800	0.16	1.2	−80	1140	10.2	−30	4770	7.5	890	11 800
PKS 0230–051	0.30	4400–5200	126	41.5	5100 ± 490	1370 ± 740	190 ± 170	70 ± 140	40 ± 180	0.26 ± 0.12	0.30 ± 0.05	7.8	3200	0.19	0.6	−30	340	15.7	−80	3880	25.8	2140	12 900
3C 94[(1)]	0.82	4150–5100	48	44.6	5480 ± 290	6 30 ± 350	200 ± 150	120 ± 150	90 ± 200	0.14 ± 0.08	0.40 ± 0.05	14.7	5200	0.34	13.7	−330::	1570	28.9	−30:	4960	15.7	5 400	12 500
PKS 0420–01[(1)]	0.70	4400–5100	42	28.9	4110 ± 330	250 ± 250	60 ± 120	30: ± 110	10: ± 150	0.07 ± 0.06	0.4 ± 0.1	14.4	5000	0.50	1.9	80:	860	16.2	−20:	3600	12.7	2360	12 200
3C 179	0.17	4400–5050	62	11.4	3570 ± 350	1160 ± 440	500 ± 120	410 ± 100	390 ± 120	0.22 ± 0.16	0.31 ± 0.05	4.3	5000	0.37	0.5	−10	620	4.0	310	2620	7.4	1460	8300
3C 380	0.68	4400–5200	86	61.9	5740 ± 750	2580 ± 470	780 ± 250	400 ± 150	320 ± 190	0.4 ± 0.08	0.28 ± 0.04	8.5	4800	0.14	6.7	20	1200	23.1	60	4000	38.8	3630	10 600
S5 1856 + 73	0.72	4400–5500	135	102.4	5730 ± 560	1350 ± 540	530 ± 190	380 ± 150	340 ± 200	0.2 ± 0.12	0.33 ± 0.05	12.3	2600	0.12	5.1	80	750	52.4	370	5300	50.0	2420	13 300
PKS 2208–137	0.47	4400–5500	54	27.8	3850 ± 300	360 ± 180	230 ± 100	190 ± 100	180 ± 140	0.07 ± 0.09	0.43 ± 0.05	12.6	4900	0.46	0.1::	70::	490::	18.1	160	3590	9.7	5380	12 100
PKS 2344 + 09	1.34	4400–5500	108	151.9	4150 ± 380	350 ± 370	40 ± 130	−20 ± 110	−30 ± 150	0.11 ± 0.11	0.35 ± 0.05	42.9	3500	0.28	10.6	−250:	880	70.0	−30	3640	81.9	1530	13 400

Column 2 is in units of 10^{-15} ergs s^{-1} cm^{-2} Å^{-1}. Columns 3 and 4 are in units of Å. Columns refereed to intensities as Columns 5, 13, 16, 19, and 22 are in units of 10^{-15} ergs s^{-1} cm^{-2}. Columns refereed to centroid velocities at different fractional intensities, FWHM, and shift as Columns 6–10, 14, 17–18, 20–21, and 23–24 are in units of km s^{-1}. (1) Centroid and peak shift determinations might be affected by the presence of a telluric band from 9250 to 9700 Å at observed wavelengths. Values ending with a colon (:) means that the values are highly uncertain and '::' that the feature is poorly defined.

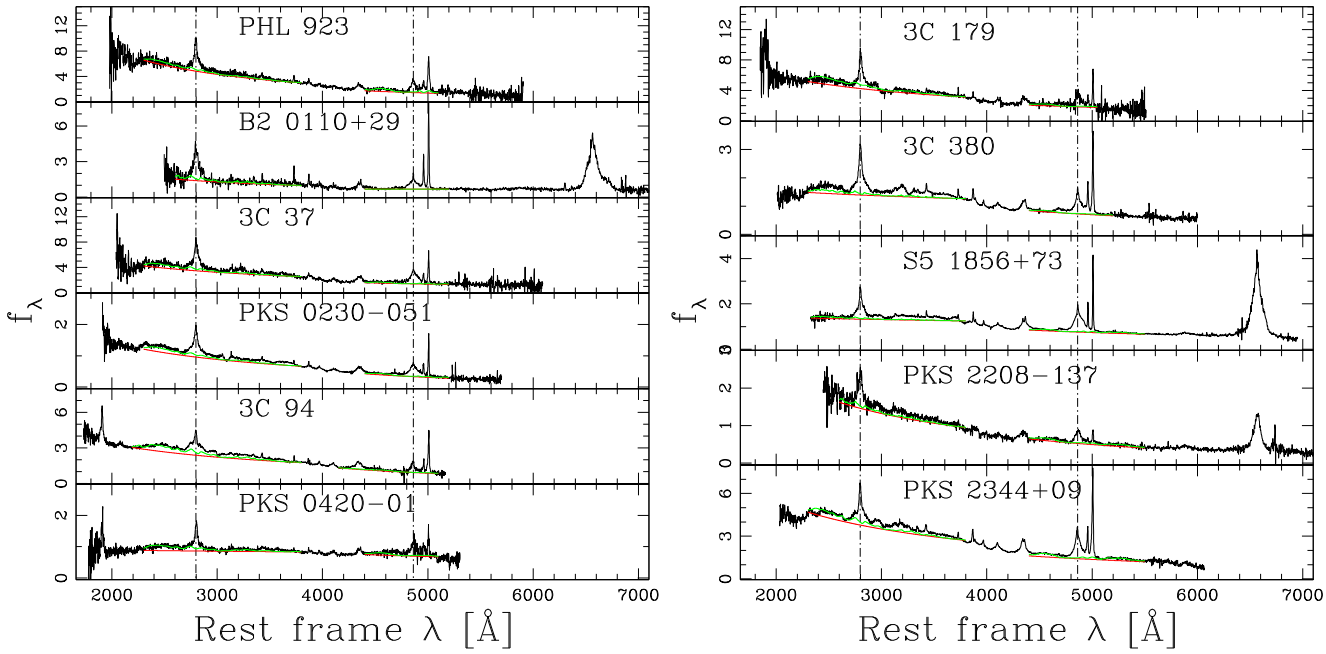

Figure 2. Rest-frame spectra of our 11 type 1 AGN, with MgII and Hβ regions after joining the two observed spectra. Abscissas are rest-frame vacuum wavelengths in Å and ordinates are specific flux in units of 10^{-15}ergs s^{-1} cm^{-2} Å^{-1}, except for PHL 923, B2 0110 + 29, 3C 37, and 3C 179 that are in units of 10^{-16}ergs s^{-1} cm^{-2} Å^{-1}. In each panel, the green line traces FeII emission and the red one represents the power-law continuum. Dot–dashed vertical lines trace the rest-frame wavelength of Hβ and MgII.

ratio I([O III]λ4959Å)/I([O III]λ5007Å) of 1:3 (Dimitrijević et al. 2007). In all sources except PHL 923, 3C 94, and PKS 2344 + 09, the HeIIλ4686Å line contributes to the blue wing of Hβ, and we constrained the shift and FWHM of the HeIIλ4686Å VBC to be the same as Hβ VBC (Snedden & Gaskell 2007).

The power law that defines the continuum level and the FeII contribution obtained from the `specfit` analysis are plotted in Fig. 2 as red and green lines respectively. The plot of the other components from the `specfit` fitting for Hβ and [O III] is presented in the right plots of Fig. 3, where the black line represents the rest-frame spectrum and the dashed magenta line shows the model fit. Residuals from the fittings are shown in the bottom panels. In 3C 94, PKS 0420–01, and 3C 179, with the highest redshift in the sample, the Hβ region is close to the edge of the observed spectrum and thus affected by more noise. This resulted in larger uncertainties in the determination of parameters related to the Hβ line profile.

3.1.2 UV region

The doublet MgII is located in a complex spectral region of the UV known as the small blue bump (e.g. Antonucci 2012; Popović, Kovačević-Dojčinović & Marčeta-Mandić 2019; Gaskell et al. 2022). To determine the parameters of the broad MgII line profiles, we carried out, as in optical, a multicomponent fitting of the region of interest including:

(i) A power-law continuum underlying MgII, in order to approximate the thermal accretion disk emission in UV region (e.g. Malkan & Oke 1983);

(ii) An FeII scalable template for accounting the $\mathrm{FeII_{UV}}$ (which is the integrated flux over 2200–3090 Å) emission lines blended with MgII. This template is based based on CLOUDY simulations assuming ionization parameter $\log U = -2.25$, $\log n_{\mathrm{H}} = 12.25$, solar chemical abundances and standard (i.e. Mathews & Ferland 1987) AGN continuum. For practical purposes it is analogous to the e.g. Bruhweiler & Verner (2008) 'best' template;

(iii) A UV Balmer continuum,
found to be important at $\lambda < 3646$Å (Kovačević, Popović & Kollatschny 2014; Kovačević-Dojčinović, Marčeta-Mandić & Popović 2017).

(iv) As MgII is a doublet, we fitted the blended line component by using multiple Gaussians:

(a) Two NCs, accounting for the doublet of MgII at λ2796.35Å and λ2803.53Å, with an assumed ratio of 1.5:1.

(b) Two BCs, where the intensity ratio between the blue and red broad component of the doublet is taken to be 1.25, which is representative of the physical conditions observed in the BLR according to CLOUDY simulations (see details in Marziani et al. 2013).

(c) One VBC, instead of two due to the small doublet separation of ∼8 Å, which is much less than the FWHM of the VBC components. This restrains us from separating two VBCs with the spectral resolution we have.

The fitting was done in a wide wavelength range, from 2600 to 3800 Å in order to include the narrow LIL [OII]λ3727Å and to obtain measurements for FeII emission in UV, which is not well known for jetted sources (Marziani et al. 2018). We also included a Gaussian profile fitting for OIIIλ3133Å and the two HILs of [NeV] at λλ3346,3426ÅÅ when the lines are clearly present. For the low redshift quasars, with z < 0.4 (B2 0110 + 29 and PKS 2208–137), the MgII doublet measures are affected by a higher uncertainty because it is located at the extreme blue edge of the observed spectrum, which could imply usually more noise and a worse determination of the blue continuum level.

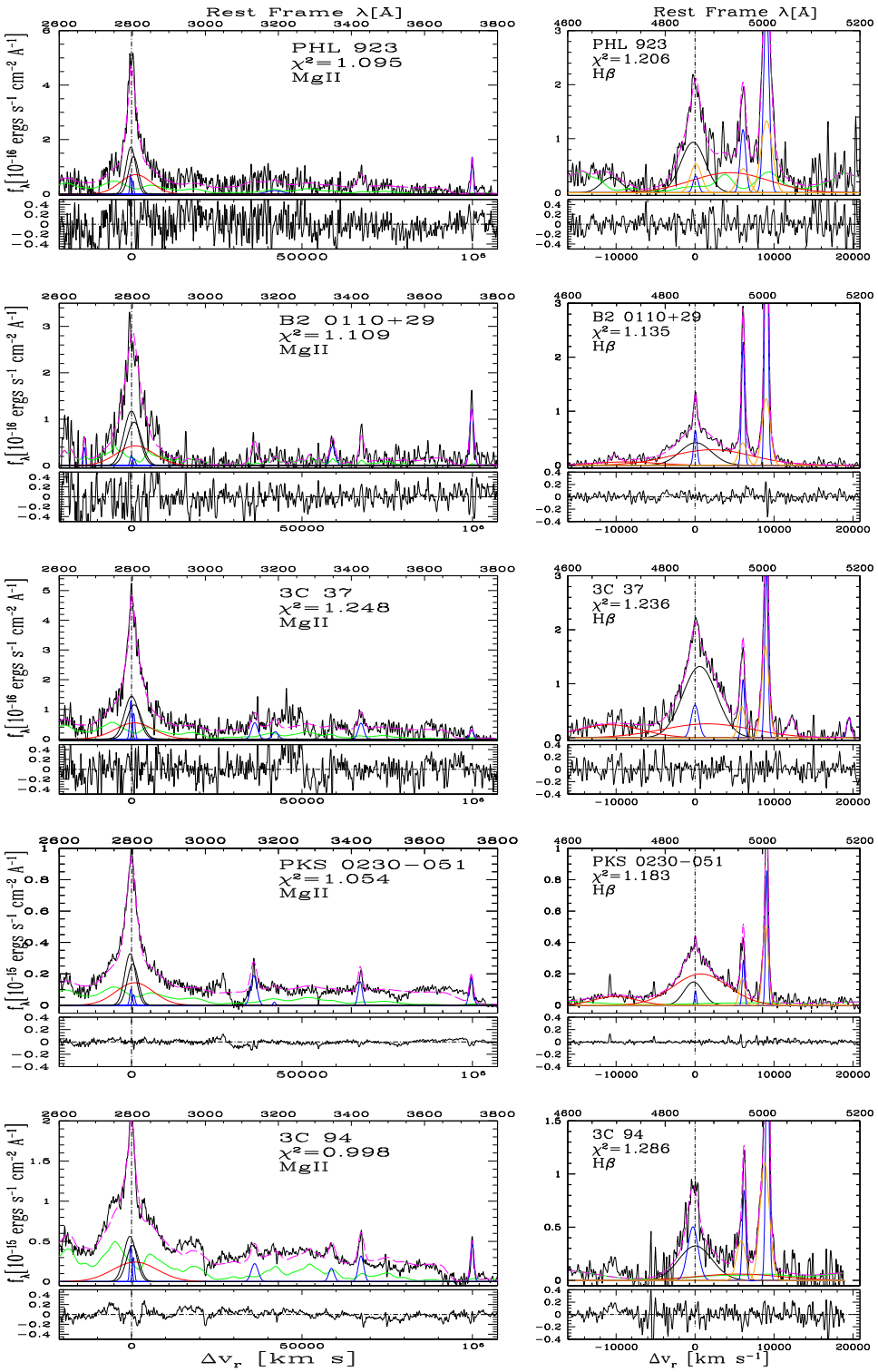

Figure 3. Multicomponent fitting results of our quasars in the region of MgII and Hβ lines (adjacent left-hand and right-hand panels), represented after subtracting the continuum obtained from the simultaneous best `specfit` fit. In both cases, the upper abscissa is rest-frame wavelength in Å and the lower abscissa is in radial velocity units. The vertical scales correspond to the specific flux in units of 10^{-15} ergs s^{-1} cm^{-2} Å^{-1} and 10^{-16} ergs s^{-1} cm^{-2} Å^{-1} (PHL 923, B2 0110 + 29, 3C 37, and 3C 179) in both panels. Black continuous lines correspond to the rest-frame spectrum. The emission line components are: FeII (green), VBC (red), BC (black), all the NCs as blue lines, and [O III] SBC as orange line. The dashed magenta line shows the model fitting. The dot–dashed vertical lines trace the rest-frame wavelength of MgII and Hβ. The lower panels show the residuals of the fit. The reduced χ^2 values indicated in each panel are estimated in a window of λ around the main lines, Hβ and MgII.

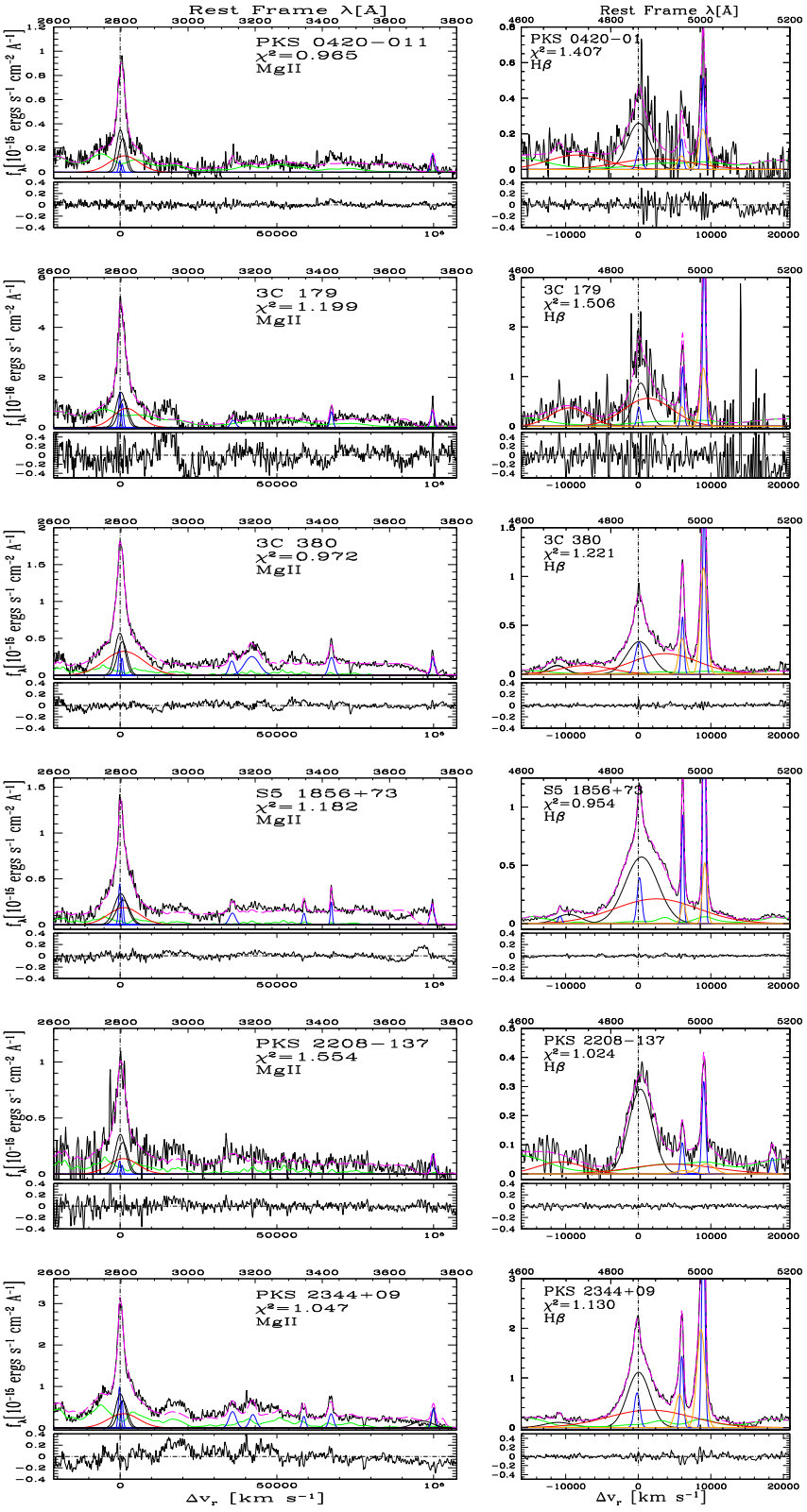

Figure 3. Results of the `specfit` analysis (cont.).

The overall fitting result for Mg II spectral region for each object is shown in the left plots of Fig. 3 (adjacent with the Hβ fitting, in the right-hand panels). Residuals from the fittings are also shown in the bottom pan

3.2 Full profile analysis

Besides the multicomponent spectral fitting to account for the individual components of the emission lines of Hβ and MgII regions,

a complementary measurement that describes the FP is required. The parametrization of the FP has been obtained by estimating the equivalent width (EW), FWHM, centroids at different fractional line intensities, ($c(i/4)$ for i = 1, 2, and 3), the peak velocity assumed to be the centroid at 9/10 fractional intensity ($c(9/10)$), and asymmetry (AI) and kurtosis (KI) indexes. The latter two quantities and centroids are used as defined according to Zamfir et al. (2010).

3.3 Error estimation

We made a coarse estimate of the fractional errors in the fluxes and relative intensities of the lines by using the interactive `IRAF` task `splot`. We empirically define extreme levels for line base or for continuum placements and assign them a confidence limit of $\pm\ 2\sigma$. The range of uncertainty and the typical errors that we derived depend on whether a feature was extended (such $\mathrm{FeII_{opt}}$ and $\mathrm{FeII_{UV}}$ emission) or sharp and prominent ([O III] narrow lines) or faint affected by a much stronger line component (i.e. HeIIλ4686Å). Considering $\mathrm{FeII_{opt}}$ emission, the uncertainty ranges between 20 per cent and 50 per cent at 1σ confidence level, the latter for quasars with extremely faint FeII emission like B2 0110 + 29. For $\mathrm{FeII_{UV}}$, we have uncertainties between 15 per cent and 35 per cent, the latter for relatively faint quasars. The Balmer continuum is affected by a comparable fractional uncertainty, as it is modelled over the same spectral range of $\mathrm{FeII_{UV}}$ emission. Considering the individual components of Hβ, the NC has uncertainties between 15 per cent and 50 per cent. The larger uncertainty applies to the case where the NC is weaker i.e. for quasars like 3C 179 and S5 1856 + 73: a small change of the BC translates into a much larger fractional change for the NC. This can also be seen from the intensity ratio between the NC and BC. For the two quasars with larger uncertainties (3C 179 and S5 1856 + 73), this ratio is, $\mathrm{I_{NC}/I_{BC}}\ \approx 0.125$ and 0.097, respectively. The prominent BC of Hβ is affected by a small uncertainty between 10 per cent and 20 per cent. For the sharp, narrow, and well-defined [O III] line, the uncertainty in flux is between 5 per cent and 10 per cent. For the UV lines, the MgII NC, in most cases we have uncertainties between 15 per cent and 30 per cent. The larger uncertainty is associated with cases in which the NC merges with the BC. For the prominent MgII BC, the uncertainty is estimated between 10 per cent and 20 per cent. The uncertainties for the BC can also be used for the VBC since the two components are usually of comparable strength.

In all the cases, errors for the FP parameters have been estimated taking into account the effect of variation in the continuum on the profile parameters, by assuming a $\pm$ 5 per cent variation in the continuum. The uncertainties were derived with quadratic error propagation.

4 RESULTS

4.1 Spectral multicomponent fitting results

4.1.1 Hβ and [O III]region

Spectrophotometric measurements of the optical region as well as the parameters of the FP and the individual components of Hβ, represented in the right-hand panels of Fig. 3, are presented in Table 4. Column 2 contains the rest-frame specific continuum flux at 5100 Å obtained from the fitted power law; Column 3 lists the wavelength range used for the spectral fitting in the Hβ region; Columns 4 to 12 report the FP measures $\mathrm{H\beta_{FP}}$ (BC + VBC): EW (Column 4), total intensity (Column 5), FWHM of $\mathrm{H\beta_{FP}}$ (Column 6), the centroids at $\frac{1}{4}$, $\frac{1}{2}$, $\frac{3}{4}$, and $\frac{9}{10}$ fractional intensity of the peak (Columns 7–10), as well as AI and KI (Columns 11 and 12, respectively). For each line component isolated with the `specfit` analysis, we report the total flux (I), the peak shift, and the FWHM in km s^{-1}: for NC (Columns 16–18), for BC (Columns 19–21), and for VBC (Columns 22–24). Additionally, we also provide in Table 4 the parameters related to FeII: the total flux of the blue blend of FeIIλ4570Å in Column 13, and the smoothing factor applied to the FeII template to reproduce the observed FeII feature (Column 14). In Column 15 we report the $R_{\mathrm{FeII,\ opt}}$ parameter (see Section 1). In the two most redshifted quasars in the sample at z > 0.9 (3C 94 and PKS 0420), the reddest part of the spectrum has a slightly lower S/N due to the correction of the telluric band that extends between 9250Å and 9700Å in the observed wavelength. This results in a kind of flat-topped and even multipeaked profile in Hβ (see Fig. 3), and slightly larger uncertainties in the determination of the higher fractional intensity centroids of Hβ, and to less extent in [O III].

Regarding $\mathrm{H\beta_{FP}}$, in general the objects of our eRk sample show FWHM(Hβ) $\gtrsim$ 4000 km s^{-1}, with a median value of 5100 km s^{-1}, which is a typical value of B1 ST quasars at z < 1 (see Section 4.2) with similar luminosities (e.g. Sulentic et al. 2002; Zamfir et al. 2008). In two cases (3C 179 and PKS 2208–137), the FWHM is slightly less than 4000 km s^{-1}. For PKS 2208–137, the barely lower value may be caused by the uncertainty in identifying the Hβ NC, which may have been included in the BC producing a slightly narrower and sharper BC profile. In the case of 3C 179, with the lowest FWHM ($\sim$ 3600 km s^{-1}) in the eRk sample, that value may be influenced by a slightly high continuum location on the red side due to the correction of the telluric band in that region, preventing an accurate continuum determination on the redward [O III].

In our quasars, the $\mathrm{H\beta_{FP}}$ presents an asymmetry towards the red, with a median AI of 0.2, which is related to the presence of a VBC. This fact is clearly reflected in the centroid velocities at different fractional intensities (see Table 4), which are significantly shifted to the red wing of the broad profile in the majority of quasars, being more pronounced towards the base of the line, with a median value of + 1160 km s^{-1}. This is also verified in the centroid velocity at half peak intensity, c($\frac{1}{2}$), with a median value of 230 km s^{-1}.

The multicomponent analysis corroborates the result obtained in the FP. In all cases, a VBC needs to be included (apart from the BC) to account for the observed Hβ profile. The contribution of the VBC represents in 4/11 quasars more than 60 per cent of the total intensity of $\mathrm{H\beta_{FP}}$ (for the whole sample the median value for VBC contribution is 57 per cent) and that reaches FWHM(VBC) $\gtrsim$ 10000 km s^{-1}. As a consequence of the presence of the VBC, FWHM($\mathrm{H\beta_{BC}}$) is always smaller than the one corresponding to the FP. The ratio between both $\xi = \mathrm{FWHM(H\beta_{BC})/FWHM(H\beta_{FP})}$ has a mean value of 0.83 ± 0.09 for our quasars, in agreement with the values reported by Marziani et al. (2013) for an SDSS composite spectrum of sources belonging to Pop. B, B1 ST quasars. Also, a NC is detected in all quasars, although in general, its intensity relative to the broad profile is small, with a median value of 6 per cent. Considering the individual components of Hβ, both the NC and BC are almost always unshifted and centered around the rest-frame of each object. In 3C 94 and PKS 2344 + 09 the NC appears slightly blueshifted. Two factors may be contributing to the shift: the first one and more probable is the possible presence of an unresolved SBC included in the NC of Hβ, in correspondence with the observed SBC of [O III] (see below), which would also explain the relatively high value obtained for the FWHM $\mathrm{H\beta_{NC}} \sim$ 1600 km s^{-1} for 3C 94. A second factor to take into account in the case of 3C 94, as we mentioned previously, is that both the Hβ profile and the FeII blue blend are affected by a telluric band extending between $\approx$ 9250 and 9700 Å in observed wavelengths (that correspond to $\sim$

4700– 4900 Å in the rest-frame), whose correction can also introduce greater uncertainty in the determination of the position of the peak and the centroids at the highest fractional intensities.

A similar analysis was carried out for [O III], as described in Section 3.1.1. The results for the FP and the individual components for [O III] λ5007Å are reported in Table 5. We present the EW (Column 2), total intensity (Column 3), FWHM (Column 4), centroid velocities at different fractional intensities (Columns 5–10), AI (Column 9), and KI (Column 10). Intensity, shift, and FWHM from the `specfit` analysis are also presented for the NC (Columns 11–13), and the SBC (Columns 14–16) of each quasar. The resulting measurements for [OIII]λ4959Å can be found by using appropriate line ratios detailed in Section 3.1.1.

Our sources show strong [O III], lines clearly separated from Hβ, presenting a spectrum characteristic of Pop. B quasars as listed in Table 5. The FP of [O III] shows a slight blue asymmetry for most of the objects, with a negative AI and a median value of −0.1. This is due to the presence of a weaker SBC that is blueshifted (for 9/11 of our sources). As can be seen in Table 5 where the `specfit` measures are presented, while the NC is, within the uncertainties, unshifted in the rest-frame of the objects, the SBC appears blueshifted with a median shift of -130 km s^{-1}, and a slightly broader FWHM of around 1100 km s^{-1}. The presence of blueshifts in HILs like [O III] is considered as one of the main detectors of outflowing gas (e.g. Zamanov et al. 2002; Komossa et al. 2008; Zhang et al. 2011; Marziani et al. 2016; Vietri et al. 2020; Deconto-Machado et al. 2022; Kovačević-Dojčinović et al. 2022). Our quasars present moderate [O III] blueshifts, indicating perhaps the presence of outflows in the inner NLR. In no case do we have the named 'blue-outlier', which is defined by a blueshift in [O III] larger than −250 km s^{-1} (Zamanov et al. 2002) and are preferentially observed at low-z in the Pop. A quasars of the MS.

In some objects-, HeIIλ4686Å is also detected in the blue side of Hβ as a residual emission in the fit. We have fitted it with a Gaussian profile. In the majority of the cases, it seems to correspond to a VBC, but in some cases, it is not clear whether this extra emission is actually HeIIλ4686Å or corresponds to the FeII blend. Only in the case of 3C 380, two components (BC and VBC) can be identified, and for PKS 0230–51, an NC is clearly seen overlaid on the VBC (see Fig. 3). The results of the `specfit` analysis for HeIIλ4686Å are reported in Table 6. The values given in the table are only to be considered, for most objects, as an indication of the HeIIλ4686Å detection.

4.1.2 *MgII region*

The results of the spectrophotometric measurements for MgII region and measured parameters including both MgII FP and the individual components from the `specfit` analysis (plotted in left panels of Fig. 3), following the approach described in Section 3.1.2, are presented in Table 7. Columns 2 and 3 contain respectively the rest-frame specific continuum flux at 3000 Å, obtained from the fitted power law, and the Balmer continuum whose intensity was estimated at the Balmer edge at 3646 Å. From Columns 4–12 are reported the FP measurements of MgII, including 2BC and a VBC: EW (Column 4), total intensity (Column 5), FWHM of MgII$_{FP}$ (Column 6), the centroids at $\frac{1}{4}$, $\frac{1}{2}$, $\frac{3}{4}$, and $\frac{9}{10}$ fractional intensity of the peak (Columns 7–10), as well as the AI and KI in Columns 11 and 12, respectively. The `specfit` fitting parameters of the individual components of the reddest line of the doublet are reported from Columns 16–24. The corresponding measures of the blue component of Mg II, can

Table 5. Results of FP and the `specfit` analysis for [OIII]λ5007Å.

Object	Full broad profile (FP)(NC + SBC)								NC			SBC		
	EW	I	FWHM	C($\frac{1}{4}$)	C($\frac{1}{2}$)	C($\frac{3}{4}$)	C($\frac{9}{10}$)	AI	KI	I	Shift	FWHM	I	Shift	FWHM
(1)	(2)	(3)	(4)	(5)	(6)	(7)	(8)	(9)	(10)	(11)	(12)	(13)	(14)	(15)	(16)
PHL 923	64	8.9	860 ± 80	−40 ± 50	−50 ± 30	−50 ± 30	−50 ± 40	0.04 ± 0.12	0.42 ± 0.04	4.99	−30	806	3.86	10	1640
B2 0110 + 29	117	7.9	480 ± 40	−40 ± 20	−40 ± 10	−40 ± 10	−40 ± 20	−0.04 ± 0.09	0.42 ± 0.05	5.24	−20	430	2.7	−60	1200
3C 37	41	5.6	580 ± 50	−100 ± 40	−60 ± 20	−50 ± 20	−40 ± 20	−0.17 ± 0.09	0.38 ± 0.04	2.41	−20	440	3.23	−150	980
PKS 0230–051	37	11.4	450 ± 40	−40 ± 30	20 ± 20	30 ± 10	40 ± 10	−0.21 ± 0.13	0.37 ± 0.04	4.94	40	340	6.5	−130	690
3C 94	57	49.1	620 ± 60	−70 ± 80	70 ± 20	90 ± 20	90 ± 20	−0.29 ± 0.20	0.32 ± 0.05	22.0	110	490	27.1	−240	1380
PKS 0420–01	14	9.7	620 ± 50	−140 ± 50	−130 ± 20	−130 ± 20	−120 ± 30	−0.02 ± 0.28	0.39 ± 0.05	4.56	−110	500	5.1	−160	1280
3C 179	27	4.8	520 ± 40	10 ± 30	20 ± 10	30 ± 10	30 ± 20	−0.09 ± 0.13	0.41 ± 0.05	2.74	20	440	2.1	−80	940
3C 380	50	36.1	610 ± 50	−30 ± 40	−10 ± 20	−10 ± 20	−10 ± 20	−0.04 ± 0.09	0.38 ± 0.05	14.4	10	470	21.7	−60	1070
S5 1856 + 73	34	25.3	410 ± 30	10 ± 20	1 ± 10	1 ± 10	10 ± 20	0.05 ± 0.06	0.44 ± 0.05	18.3	30	370	7.0	120	760
PKS 2208–137	7	3.4	600 ± 40	−70 ± 20	−60 ± 20	−50 ± 20	−50 ± 20	−0.12 ± 0.07	0.45 ± 0.04	2.43	20	530	1.0	−210	620
PKS 2344 + 09	63	85.3	660 ± 60	−270 ± 80	−160 ± 20	−140 ± 20	−130 ± 30	−0.23 ± 0.25	0.34 ± 0.05	39.6	−100	520	45.7	−400	1300

Column 2 is in unit of Å. Columns 3, 11, and 14 are in units of 10^{-15} erg s^{-1}cm^{-2}. Columns 4–8, 12–13, and 15–16 are in units of km s^{-1}.

Table 6. `Specfit` result of HeIIλ4686Å.

Object	BC			VBC		
	I	Shift	FWHM	I	Shift	FWHM
(1)	(2)	(3)	(4)	(5)	(6)	(7)
PHL 923	1.5	160	3190	–	–	–
B2 0110 + 29	–	–	–	1.0	2070	9630
3C 37	–	–	–	4.0	990	9600
PKS 0230–051	–	–	–	8.7	2180	10 310
3C 94	–	–	–	–	–	–
PKS 0420–01	–	–	–	13.2:	2410:	9730:
3C 179	–	–	–	3.9	1510	6660:
3C 380	4.5	−420	3070	12.7	3670	8470
S5 1856 + 73	5.3	1200	4060	–	–	–
PKS 2208–137	–	–	–	4.6	540	7110
PKS 2344 + 09	8.2	−260	4760	–	–	–

Columns 2 and 5 are in units of 10^{-15} ergs s^{-1}cm^{-2}. Columns 3, 4, 6, and 7 are in km s^{-1}. For (:) measurements see the notes in Table 4.

easily be found by taking into account the appropriate line ratio (see Section 3.1.2). For each red line component analysed, we report the total flux (I), the peak shift, and the FWHM of the NC (Columns 16–18), BC (Columns 19–21), and VBC (Columns 22–24). In addition, we also provided the parameters related to FeII$_{UV}$: the total flux of the blue blend (Column 13), and the smoothing factor applied to FeII$_{UV}$ template to reproduce the observed FeII feature (Column 14). In Column 15, we report the $R_{FeII,\,UV}$ parameter, i.e. the ratio between the intensities of FeII$_{UV}$ (in the 2200–3090 Å range) and MgII ($R_{FeII,\,UV}$ = I(FeII$_{UV}$)/I(MgII$_{FP}$)).

As in the case of Hβ, the FWHM of MgII FP is higher than FWHM of MgII BC obtained from the `specfit` analysis. The median value for the ratio ξ_{Mgii} = FWHM(MgII$_{BC}$)/FWHM(MgII$_{FP}$) is 0.84 ± 0.02 for our quasars, in good agreement with the value found by Marziani et al. (2013) for the ST B1 by using composite spectra. This is due to the presence also of a VBC in MgII, with a FWHM $\gtrsim$ 10 000 km s^{-1}, though MgII shows a weaker VBC, with a median flux representing about the 42 per cent of the total broad intensity. This manifests itself in a redward asymmetry, although showing a more symmetric profile than Hβ, with <AI> = 0.04, and a shift towards the red of the centroid velocities of MgII, more pronounced towards the base of the line, with <c($\frac{1}{4}$)> ≈ 300 km s^{-1}.

In addition, Table 8 presents the parameters obtained from the fit to a single Gaussian profile of other lines detected in the UV region, such as the OIIIλ3133Å, HIL [NeV]λ3426Å and [OII]λ3728Å doublet. For each of these lines the total flux, the peak shift, and FWHM are reported when the corresponding line is detected in the spectrum.

4.2 Main sequence optical plane

The optical plane of the 4DE1 parameter space is defined by the Hβ_{FP} FWHM and $R_{FeII,\,opt}$. The quasar MS allows contextualization of the observed empirical spectroscopic properties of type I AGN and their connection with the physical conditions of the BLR (see e.g. Sulentic et al. 2000a; Marziani et al. 2018; Panda et al. 2019b; Wolf et al. 2020). After performing the analysis of the Hβ region (see Section 4.1.1), that provides us with both the FWHM(Hβ_{FP}) and R_{FeII} (Table 4 Columns 6 and 15, respectively), we can locate our quasars in the MS. It is possible to subdivide the optical plane into a grid of bins (or STs) formed from FWHM(Hβ_{FP}) and $R_{FeII,\,opt}$ that shows different spectral line profile properties (Sulentic et al. 2002): bins A1 to A4 are defined in terms of increasing $R_{FeII,\,opt}$

Table 7. Measurements of the MgII region.

			Full broad profile parameters (FP) (2BC + VBC)							FeII$_{UV}$		NC(red)			BC(red)			VBC(red)		
Object	$f_{\lambda,\,3000Å}$	$f_{\lambda,\,3646Å}$	EW	I	FWHM	C($\frac{1}{4}$)	C($\frac{1}{2}$)	C($\frac{3}{4}$)	C($\frac{9}{10}$)	AI	KI	I	SF	$R_{FeII,\,UV}$	I	Shift	FWHM	I	Shift	FWHM	I	Shift	FWHM
(1)	(2)	(3)	(4)	(5)	(6)	(7)	(8)	(9)	(10)	(11)	(12)	(13)	(14)	(15)	(16)	(17)	(18)	(19)	(20)	(21)	(22)	(23)	(24)
PHL 923	0.43	0.02	37	17.9	4000 ± 320	120 ± 300	20 ± 180	−10 ± 150	0.05 ± 0.12	0.41 ± 0.05	25.7	4660	1.44	0.2	−130	480	4.6	10	3370	7.6	1070	10 610
B2 0110 + 29	0.13	0.02	118	16.3	5810 ± 450	250 ± 280	190 ± 160	170 ± 150	160 ± 210	0.02 ± 0.09	0.42 ± 0.05	10.9	2490	0.67	0.1	150	890	4.8	180	5130	5.5	940	13 010
3C 37	0.32	0.03	57	19.8	5600 ± 440	250 ± 280	210 ± 160	200 ± 150	200 ± 210	0.02 ± 0.09	0.42 ± 0.05	29.1	4170	1.47	0.7	50	850	5.6	220	4910	7.2	650	13 140
PKS 0230–051	0.88	0.07	42	40.5	4470 ± 360	−40 ± 280	−130 ± 130	150 ± 120	160 ± 160	0.03 ± 0.13	0.40 ± 0.05	65.7	5720	1.62	0.6	30	890	9.8	−220	3750	18.5	750	12 910
3C 94	2.22	0.19	34	79.9	5000 ± 410	−60 ± 320	−160 ± 140	180 ± 130	190 ± 180	0.03 ± 0.09	0.40 ± 0.05	247::	3560	3.09	2.2	−30	750	18.8	−270	4230	37.4	1050	15 460
PKS 0420–01	0.86	0.07	40	33.9	3600 ± 190	330 ± 210	260 ± 100	240 ± 100	240 ± 130	0.02 ± 0.28	0.41 ± 0.05	85.8	5720	2.53	0.5	50	870	8.4	260	3010	15.1	1120	11 140
3C 179	0.40	0.03	40	16.7	4410 ± 360	830 ± 280	600 ± 130	550 ± 120	540 ± 160	0.10 ± 0.13	0.40 ± 0.05	46.9	6840	2.81	0.8	120	830	4.6	460	3630	7.6	1880	10 000
3C 380	1.36	0.16	61	85.3	4610 ± 400	320 ± 420	140 ± 140	120 ± 120	110 ± 170	0.07 ± 0.09	0.37 ± 0.05	59	2490	0.69	1.9	20	850	16.7	110	3680	47.8	1070	14 750
S5 1856 + 73	1.31	0.16	39	51.2	5770 ± 460	530 ± 310	430 ± 160	400 ± 150	390 ± 210	0.03 ± 0.06	0.41 ± 0.04	35.9	2490	0.70	2.8	60	900	13.1	410	4870	21.7	1100	11 630
PKS 2208–137	1.32	0.07	27	39.4	4440 ± 350	300 ± 240	240 ± 120	230 ± 120	220 ± 160	0.04 ± 0.07	0.42 ± 0.04	45.3	2490	1.15	0.7	20	860	10.7	270	3810	15.2	870	11 100
PKS 2344 + 09	3.46	0.21	25	92.1	4240 ± 340	400 ± 240	340 ± 120	320 ± 110	320 ± 160	0.04 ± 0.25	0.41 ± 0.05	271	3020	2.94	5.8	0	890	29.2	270	3580	39.5	910	11 530

Columns 2 and 3 are in units of 10^{-15} ergs s^{-1} cm^{-2} Å^{-1}. Column 4 is in units of Å. Columns 5, 13, 16, 19, and 22 are in units of 10^{-15} ergs s^{-1} cm^{-2}. Columns 6–10, 14, 17–18, 20–21, and 23–24 are in units of km s^{-1}. Columns 16–24 show measurements of the red component of MgII doublet. Measurements of the blue component can be obtained by using the line ratios given in Section 3.1.2.

Table 8. `Specfit` analysis results for the other UV lines.

Object	OIIIλ3133Å			[NeV]λ3426Å			[OII]λ3728Å		
	I	Shift	FWHM	I	Shift	FWHM	I	Shift	FWHM
(1)	(2)	(3)	(4)	(5)	(6)	(7)	(8)	(9)	(10)
PHL923	–	–	–	–	–	–	1.0	170:	550:
B2 0110 + 29	–	–	–	–	–	–	1.8	70	1130
3C37	1.2	130:	1880:	1.0	−70	1550	0.4:	70	1090::
PKS 0230–051	4.1	−110	1940	2.1:	−260:	1170:	2.6	−40	1080
3C94	4.4	110	1950	6.1	60	1560	6.1	190	1030
PKS 0420–01	–	–	–	–	–	–	2.2:	30:	1150:
3C179	0.1::	80::	1680::	0.1:	20:	940:	0.1	−20	1030
3C380	4.1::	−310::	1910::	5.0	40	1700	3.4	60	1070
S5 1856 + 73	3.0::	−150::	2150::	1.8	−1	600	3.4:	−110:	1130:
PKS 2208–137	–	–	–	–	–	–	2.6	80	1090
PKS 2344 + 09	10.4::	−110::	2380::	5.9	−70	1420	7.0:	200:	1140:

Columns 2, 5, and 8 are in units of 10^{-15} ergs s^{-1} cm^{-2}. Other columns are in km s^{-1}. For (:) and (::) measurements, see the notes in Table 4.

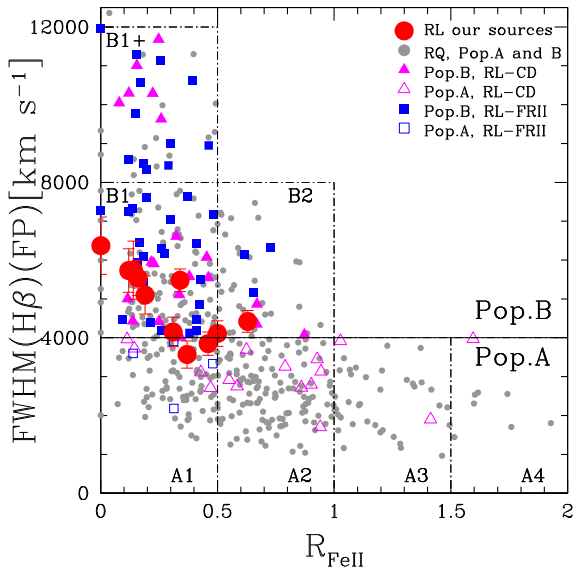

Figure 4. Location of our eRk quasars (large red solid circles) in the optical plane of the 4DE1 space, traced by the measures from the Zamfir et al. (2010) sample, where grey dots represent the RQ (Pop. A & B) and blue and magenta symbols corresponds to RLs. The horizontal line at 4000 km s^{-1} marks the nominal Pop. A - B boundary. For the explanation of different STs, see Section 4.2. The vertical axis is truncated at 12 500 km s^{-1} for clarity.

with bin size $\Delta R_{\rm FeII,\,opt} = 0.5$ (from A1 with $R_{\rm FeII} < 0.5$ to A4 with $1.5 < R_{\rm FeII} \leq 2$), while bins B1, B1^{+} and B1^{++} are defined in terms of increasing FWHM with ΔFWHM = 4000km s^{-1}, from B1 with $4000 <$ FWHM≤ 8000 km s^{-1} to B1^{++} with FWHM > 12000 km s^{-1}.

Fig. 4 shows the locus of our quasars on the MS as well as the Pop. A/B separation and the identification of some of the most populated STs, where we have also included as a comparison the low-z SDSS sample by Zamfir et al. (2010). In Fig. 4, grey symbols represent the Pop. A and B RQs, meanwhile coloured symbols represent the RLs, splited into core-dominated (CD; magenta triangles) and LD FRII (blue squares). As clearly seen in this figure, the RQ sources show a broad domain in the MS, covering the entire range of observed values in both FWHM and $R_{\rm FeII}$, and in both A and B populations. On the converse, the RL ('jetted') sources are mainly Pop. B and populate particular bins of the optical plane, mostly in B1 and B^{+} (Zamfir et al. 2008; Kuźmicz, Sethi & Jamrozy 2021).

Our quasars are well located in the MS domain of the CD RL sources. The majority lie in the B ST (more than 80 per cent), mostly in B1. For 3C 179 and PKS 2208, FWHM(H$\beta_{\rm FP}$) value is only marginally below 4000 km s^{-1} placing them on the upper edge of Pop. A, at the ST A1. Since in both quasars there is no doubt about its Pop. B classification with a clearly recognized VBC in the Hβ profile, its position may be due to an inclination effect (as we mentioned in Section 4.1.1) since the broadening of Hβ is orientation-dependent (Wills & Browne 1986; Sulentic et al. 2003; Zamfir et al. 2008). Our quasars also show weak FeII$_{\rm opt}$ intensities. All except one case (PHL 923 with $R_{\rm FeII,\,opt} = 0.63$ that locates the object in B2 bin) present low $R_{\rm FeII,\,opt}$ values, with a mean of 0.29 and a $\sigma = 0.19$. This is in agreement with the results obtained by Marziani et al. (2021) who using composite spectra found that RL sources, both CD and FRII, present weaker FeII$_{\rm opt}$ emission ($\sim$ a factor 2 lower) compared to the composite spectrum of RQ quasars sharing the same B1 ST.

4.3 Main sequence UV plane

In a close analogy to the optical plane, it is also possible to analyse the UV plane by using MgII, and FeII$_{\rm UV}$ line parameters. This is possible mainly due to the fact that both Hβ and MgII lines belong to LILs and are supposed to be emitted from a similar region (Collin-Souffrin et al. 1988). The UV plane is also formed by using MgII$_{\rm FP}$ FWHM and the strength of the FeII$_{\rm UV}$. Fig. 5 shows the location of our eRK quasars in the UV plane where we used as a comparison sample the recently available parameters determined by the software QSFIT from Calderone et al. (2017) using SDSS-DR10 spectra, in which they incorporated spectral information in the UV, and in particular for MgII and FeII$_{\rm UV}$ to produce a publicly available catalogue of AGN spectral properties. See also a discussion about this catalogue and the MS UV plane in Śniegowska et al. (2020). For the QSFIT catalogue, we selected a sample consisting of the sources in the redshift range from 0.4 to 1 and with good quality measures in MgII and FeII$_{\rm UV}$ according this catalogue. The available comparison sample is large in number (10 344 spectra), and we used therefore a kernel smoothing for better visualization. As compared to the optical plane, the UV plane shows a larger range in $R_{\rm FeII,\,UV}$. This is mainly due to the fact that the range of the integrated flux in FeII$_{\rm UV}$ is broader as compared to the optical, FeII$_{\rm opt}$. For the sole purpose

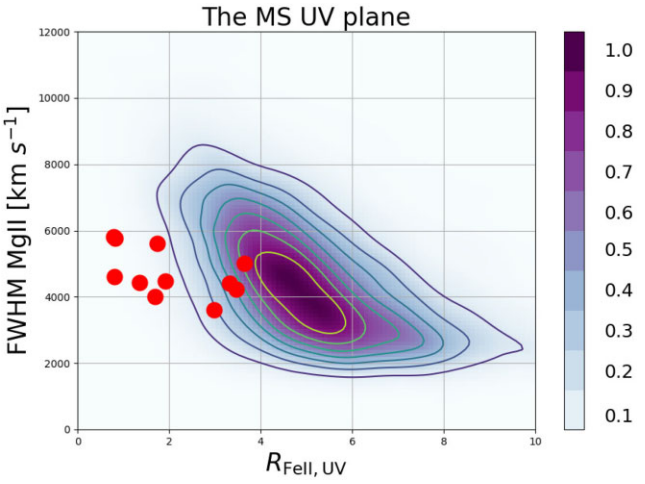

Figure 5. Location of our eRK quasars (red solid circles) in the UV plane defined by MgII FWHM and $R_{\rm FeII,\,UV}$. A comparison sample was taken from Calderone et al. (2017) catalogue by considering sources that are found around our redshift range ($0.4 \lesssim z \lesssim 1$) and is shown after kernel smoothing to account for a large number of sources (10 344). The color scale is normalized to the peak density in the UV parameter plane.

of the representation of our sample in the UV plane together with the data obtained from the QSFIT catalogue, we have estimated a $\rm FeII_{UV}$ modified total flux for our RL sources by extrapolating the $\rm FeII_{UV}$ model fitted to our spectra to the wavelength range λ1250Å to λ3090Å used by Calderone et al. (2017). Our quasars are placed in the FWHM($\rm MgII_{FP}$) $\gtrsim$ 4000 km s^{-1} and in the lowest $\rm FeII_{UV}$ emission, as in the case of the optical plane.

4.4 Comparison between the Hβ and MgII spectral ranges

4.4.1 MgII and Hβ line profiles

Based on the measurements reported in Tables 4 and 7, we analyse and compare here the line profile parameters of Hβ and MgII. The upper and bottom panels of Fig. 6 show the location of our eRk quasars in the c($\frac{1}{2}$) and c($\frac{1}{4}$) versus FWHM($\rm H\beta_{FP}$) plots, respectively. The comparison sample containing the c($\frac{1}{2}$) information for the RL and RQ was taken from Marziani et al. (2003a) and the c($\frac{1}{4}$) from Zamfir et al. (2010). Our eRk quasars are located in the upper right part of both diagrams, mainly occupied by Pop. B quasars, but showing more extreme shift values in the c($\frac{1}{4}$) when compared to Zamfir et al. (2010) sample. Fig. 6 also shows that our quasars follow the trend observed in the other two samples in the sense that larger velocity centroids, particularly in c($\frac{1}{4}$), correspond to wider FWHM($\rm H\beta_{FP}$). Similarly, Fig. 7 shows the centroid at c($\frac{1}{2}$) (upper plot) and c($\frac{1}{4}$) (lower plot) peak intensity of the MgII profile versus the FWHM of $\rm MgII_{FP}$ for our quasars and for the composite spectra by Marziani et al. (2013) corresponding to the different STs of the MS, with cyan solid triangles denoting Pop. A and orange-filled circles for Pop. B. Also in MgII our eRk objects are located in the Pop. B region and showing a larger shift towards the red in the base of the line, although it is less pronounced than in Hβ.

One of the first differences between the two lines is observed in the broadening estimator, FWHM of the FP, in which the FWHM($\rm MgII_{FP}$) is narrower than FWHM($\rm H\beta_{FP}$): the median value of $\rm MgII_{FP}$ FWHM is 4470 km s^{-1}, about 10 per cent less than the FWHM of $\rm H\beta_{FP}$, 5100 km s^{-1}. Since for the FWHM measurements of $\rm MgII_{FP}$, a single unresolved line is assumed for the doublet, those

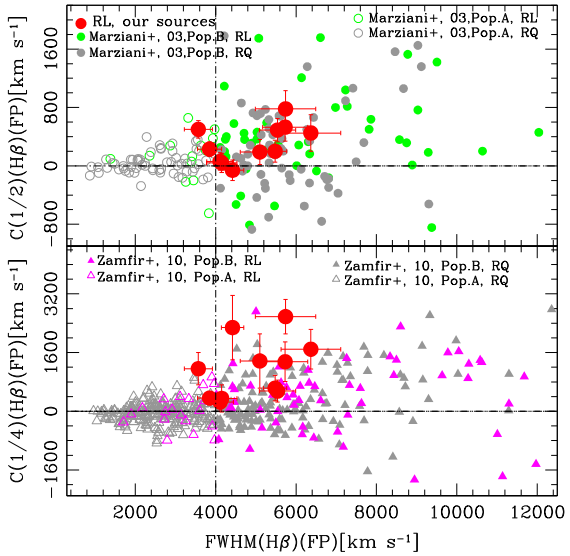

Figure 6. Centroids at $c(\frac{1}{2})$ (upper plot) and $c(\frac{1}{4})$ (bottom plot) peak intensity of $\rm H\beta_{FP}$ versus the FWHM of $\rm H\beta_{FP}$. The large red solid circles represent our RL objects. Comparison samples from Marziani et al. (2003a) and Zamfir et al. (2010) are also represented. The legends identify different populations and radio classes. The vertical dot–dashed line at 4000 km s^{-1} marks the nominal population A/B boundary. The horizontal dot–dashed line traces the symmetric line in $c(\frac{1}{2})$ and $c(\frac{1}{4})$.

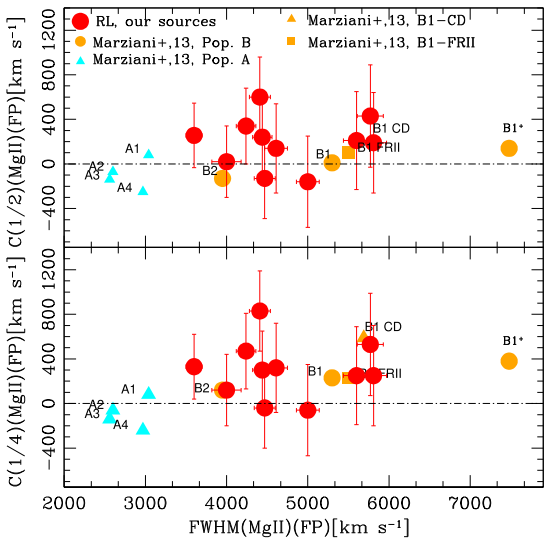

Figure 7. Relation between $c(\frac{1}{2})$ (upper) and $c(\frac{1}{4})$ (lower) versus FWHM of MgII. Red solid circles from our RL spectra. The additional comparison sample shown in the plot was taken from Marziani et al. (2013). Orange symbols represent Pop. B and cyan solid triangles for Pop. A. Orange solid triangle and square represent Pop. B CD and FRII respectively.

values can be converted to the FWHM of a single component by subtracting 300 km s^{-1} (Trakhtenbrot & Netzer 2012). Taking into account this correction, we obtained a median value for the FWHM of MgII single component of $\approx$ 4170 km s^{-1}, that corresponds to $\approx 0.84 \pm 0.12$ the median $\rm H\beta_{FP}$ FWHM, of our eRK quasars, in agreement with previous results obtained by Wang et al. (2009), claiming that FWHM of Hβ is larger than FWHM of MgII, and later clearly identified by Marziani et al. (2013) for the Pop. B quasars.

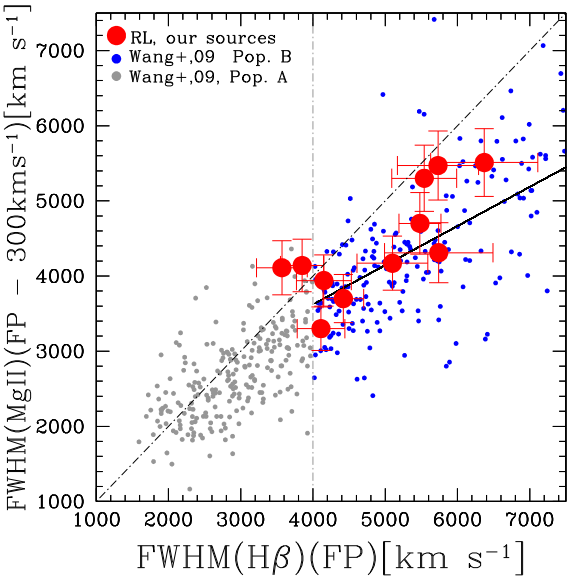

Figure 8. Comparison between MgII and Hβ FWHM. The ordinate is the FWHM of MgII$_{\rm FP}$ subtracted by 300 km s^{-1}. A comparison sample was taken from Wang et al. (2009) that we subdivided into Pop. A (grey dots) and Pop. B (blue dots) by using the 4000 km s^{-1} as a separation limit. The solid line represents the correlation of both FWHM including only Pop. B sources from Wang et al. (2009) and our quasars. The two values are highly correlated with a Pearson's correlation factor $r \approx 0.78$ and p-value ≈ 0.005.

As explained in Marziani et al. (2013), MgII might be emitted predominantly farther out from the central continuum source than Hβ. This means only part of the gas emitting Hβ is emitting MgII. For instance, the innermost regions moving with the largest velocities close to the Hβ line base could be too highly ionized to emit MgII. This is quite true as much of the broad-line emission's kinematics can be dominated by Keplerian motion (Peterson & Wandel 1999, 2000).

Fig. 8 shows the relation between FWHM of one single component of MgII and H$\beta_{\rm FP}$, along with a comparison sample built by Wang et al. (2009). This figure shows that the correlation deviates from the one-to-one line as the profile widths are affected by the VBC present in both Hβ and MgII, significantly more pronounced in Hβ, (see Sections 4.1.1 and 4.1.2). This deviation is larger for higher FWHM(Hβ) and in particular for FWHM > 4000 km s^{-1} corresponding to Pop. B sources where VBC is detected.

A second difference is observed in the FP measurements deviation from the rest-frame spectra at specified fractional intensities, mainly at c($\frac{1}{2}$) and c($\frac{1}{4}$), as we mentioned above (see also Figs 6 and 7). The results of the centroid measurements on H$\beta_{\rm FP}$ and MgII$_{\rm FP}$ indicate a shift towards the red for both lines. The shift has larger amplitude in Hβ than MgII, as shown in Fig. 9 (left-hand and middle panels). This amplitude difference becomes more evident when considering the line base: the value of c($\frac{1}{4}$) is larger than the value of c($\frac{1}{2}$), suggesting that Hβ is more strongly affected than MgII by contribution of the VBC (Sulentic et al. 2000c, 2002).

The same trend was shown when considering the AI (see Table 4 and 7, Column 11, respectively). Fig. 9 (right) indicates that both Hβ and MgII profiles show redward asymmetry, although the AI is significantly larger for Hβ than for MgII, i.e MgII is more symmetric than Hβ. Higher KI found for MgII than Hβ are explained by the broadening of the MgII line due to its doublet components separated by 300 km s^{-1} and by the broader Hβ profile at the line base.

The redward asymmetry in Hβ for Pop. B sources have been previously observed (e.g. Sulentic et al. 2002; Marziani et al. 2009; Wolf et al. 2020), and can be linked to the existence of a distinct kinematic emitting region, the VBLR. The difference in the profile shape between Hβ and MgII and the `specfit` line profile analysis provides empirical evidence that the stronger Hβ VBC gives rise to a stronger redward asymmetry than in MgII.

4.4.2 *Equivalent widths and intensities*

The EW reflects the emission line strength relative to the total continuum and was obtained in each object from the best spectral fit. Fig. 10 (left) shows the EW of FeII$_{\rm UV}$ versus the EW of FeII$_{\rm opt}$. A correlation is not found between the two quantities. This is in agreement with the previous result by Kovačević-Dojčinović & Popović (2015) who do not find any correlation between the EWs of these lines. The discrepancy could be due to a difference in the emitting regions: the FeII$_{\rm opt}$ emission is usually thought to arise in the outer BLR before the inner radius of the torus (e.g. Popović et al. 2009; Kovačević, Popović & Dimitrijević 2010; Shapovalova et al. 2012; Barth et al. 2013; Kovačević-Dojčinović & Popović 2015). The FeII$_{\rm UV}$ might be preferentially emitted in clouds closer to the continuum source and strongly affected by the X-ray emitting corona believed to be present in most AGN (Panda et al. 2019a). Excitation mechanisms are also expected to be different: FeII$_{\rm UV}$ is produced by recombination following photoionization and enhance by florescence phenomena with continuum and Lyα, while collisional excitation contributes to optical emission (see Marinello et al. 2020, for a Grotrian diagram showing the channels leading to FeII$_{\rm UV}$ and FeII$_{\rm opt}$ production by Lyα fluorescence; c.f. Sigut & Pradhan 2003). A loose correlation between the intensities of the FeII$_{\rm opt}$ and FeII$_{\rm UV}$ and $R_{\rm FeII,\ UV}$ and $R_{\rm FeII,\ opt}$ might be expected in large samples of quasars because optical and UV emissions are both dependent on chemical abundances that are widely and systematically different along the quasar MS (Panda, Marziani & Czerny 2019b; Śniegowska et al. 2021; Marziani et al. 2023).

The intensities of Hβ and MgII are highly correlated (Fig. 10, right): Pearson's $r \approx 0.77$, with a probability $P \approx 0.01$ of a stochastic correlation. The MgII/Hβ intensity ratio varies in the range 0.5–1.8, with an average of $\approx$1.2, a value consistent with the ones derived for composites RL spectra in Population B (see table 3 of Marziani et al. 2013).

5 DISCUSSION

As pointed out in the previous sections, quasars broad-line spectra show a wide range of line profiles, line shifts as well as line intensities. In order to explain this spectroscopic diversity, much emphasis was placed on the connection between profile parameters (e.g. Martínez-Aldama et al. 2015; Kovačević-Dojčinović et al. 2022; Rakić 2022), $M_{\rm BH}$ (e.g. Boroson 2002; Hernitschek et al. 2016; Bao et al. 2022), luminosity (e.g. Marziani et al. 2009; Popović & Kovačević 2011; Rakić et al. 2017) and accretion rate (e.g. Marziani et al. 2001; Mathur, Kuraszkiewicz & Czerny 2001). In this section, we present a discussion on $M_{\rm BH}$ and Eddington ratio ($\lambda_{\rm E}$) (Section 5.1), and their effects on line profile shapes (Section 5.2). Finally, we consider the role of radio loudness (Section 5.3).

5.1 Black hole mass and Eddington ratio

The estimation of $M_{\rm BH}$ and Eddington ratio ($\lambda_{\rm E}$) is crucial for understanding the AGN phenomenon, its evolution across cosmic

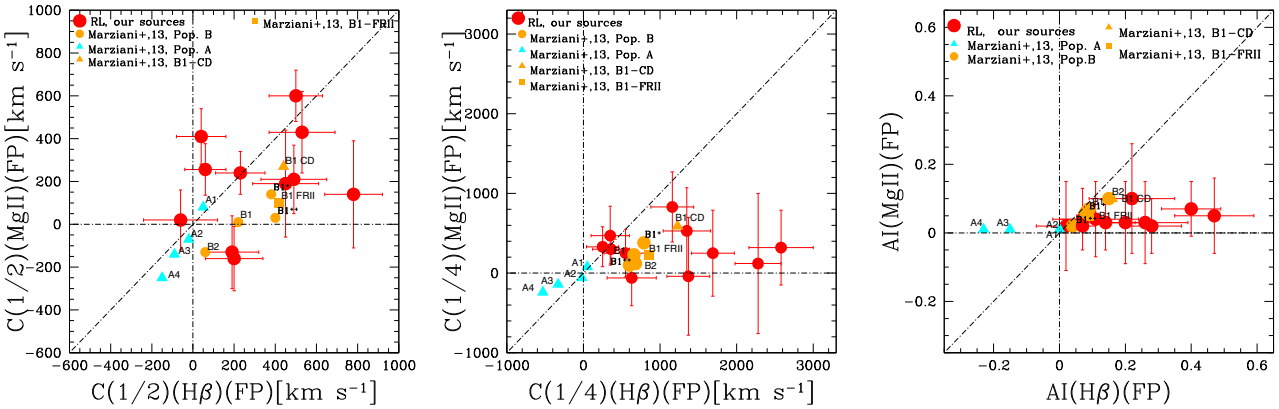

Figure 9. Comparison between Hβ and MgII c($\frac{1}{2}$) (left), c($\frac{1}{4}$) (middle) and asymmetry index (right) for our eRk quasars (red filled circles). Additional comparison sample was taken from composite spectra of Marziani et al. (2013), where symbols are as in Fig. 7. The diagonal dot–dashed line in each plot represents the one-to-one line.

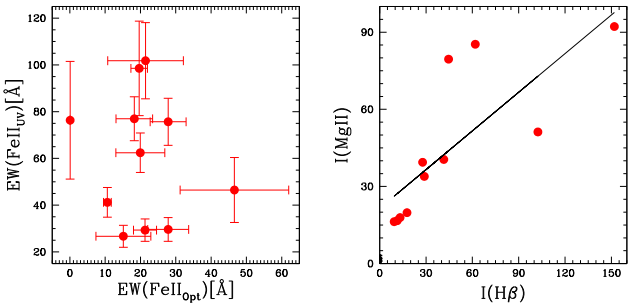

Figure 10. Left: relation between EW of $\mathrm{FeII_{opt}}$ and $\mathrm{FeII_{UV}}$. The uncertainties in the EW are taken to be proportional to the uncertainty in the flux of the FeII emissions in the two regions (see Section 3.3). Right: correlation between the intensities of Hβ and MgII. The intensities are highly correlated with $r \approx 0.77$ and a p-value ≈ 0.01.

time, and the properties of the host galaxies (e.g. Marconi & Hunt 2003). In addition, $M_{\rm BH}$ is a fundamental parameter that relates to the evolutionary stages and the accretion processes occurring within them, as the power output is directly proportional to $M_{\rm BH}$ (e.g. Lapi et al. 2006; Fraix-Burnet et al. 2017). $\lambda_{\rm E}$ is a parameter that expresses the relative balance between gravitational and radiation forces (e.g. Marziani et al. 2010; Netzer & Marziani 2010), a major factor influencing both the dynamics and the physical conditions of the line emitting gas (Marziani et al. 2018).

To estimate $M_{\rm BH}$ for type I AGN, we used an empirically calibrated formalism (scaling laws) that is based on single-epoch spectra (e.g. Vestergaard & Peterson 2006; Ho & Kim 2015) and that has been applied to large and diverse samples of AGN (e.g. Marziani & Sulentic 2012b; Shen 2013). At low redshift ($z \lesssim 0.8$), the lines of choice for estimation can be Hβ and MgII (e.g, Kaspi et al. 2000; McLure et al. 2006; Vestergaard & Peterson 2006). Table 9 reports the estimations of the accretion parameters for our eRk quasars by using both the BC and FP FWHM measurements. Columns 2 and 5 report the bolometric luminosity ($L_{\rm bol}$) estimated from the optical (5100 Å) and UV (3000 Å) contunuum luminosity respectively, as λL_{λ}, by using the luminosity-dependent relation from Netzer (2019) to calculate the bolometric correction factor (K_{bol}) for the luminosity in question (L_{5100} or L_{3000}). The bolometric luminosity of our eRk quasars estimated with $\log L_{\rm bol}$ between 45.15–46.57 and 44.98–46.53 [ergs s^{-1}] from Hβ and MgII, respectively. Columns 3–4 and 6–7 list the $M_{\rm BH}$ and $\lambda_{\rm E}$ by using the FP FWHM measures and the relations from Vestergaard & Peterson (2006) for Hβ and Trakhtenbrot & Netzer (2012) for the MgII line, respectively. The same estimation was also done by using FWHM of the BC alone rather than the FP and reported in Columns 8–11. $M_{\rm BH}$ values computed from the FP FWHM range from $\log M_{\rm BH}$ [$M_{\odot}$] $\approx$ 8.49–9.25 (Hβ) and from $\log M_{\rm BH} \approx$ 8.26–9.33 (MgII). Fig. 11 indicates that the mass estimation using Hβ and Vestergaard & Peterson (2006) relation is in a very good agreement with the mass estimation from MgII, when using four different MgII scaling laws, namely the ones from Vestergaard & Osmer (2009), Shen et al. (2011), Trakhtenbrot & Netzer (2012), and Shen & Liu (2012). This result also holds if only the BC is used (see Table 9, Columns 8 and 10). We also checked the mass estimation by using the MgII with McLure & Jarvis (2002) relation and found a lower estimation by about 0.25 dex compared to the other scaling relations (not shown in Fig. 11 to avoid confusion).

The $\log(\lambda_{\rm E})$ values for our eRk quasars range from -1.45 to -0.55 and from -1.40 to -0.78 (see Table 9, Colūmns 4 and 7) when using the Hβ and MgII lines, respectively. Previous studies suggested that around some critical value of $\lambda_{\rm E} \approx 0.2 \pm 0.1$, there could be an accretion mode change, i.e. a change in the structure of the accretion disk (e.g. Abramowicz & Straub 2014; Marziani et al. 2018; Giustini & Proga 2019, and references therein), or at least in the BLR dynamics (Collin et al. 2006). For a given $\log M_{\rm BH} \approx 8.5$, Pop. A sources show $\log(\lambda_{\rm E}) =$ -0.7–0, and Pop. B show $\log(\lambda_{\rm E}) = -2$ to -0.7 (Sulentic, Marziani & Zamfir 2011). All our quasars fit into the Pop. B domain of low accretion rates. The two sources (3C 179 and PKS 2208–137) with FWHM < 4000 km s^{-1} have $\log(\lambda_{\rm E}) \approx -0.64$ and -0.75, respectively. These values are at the $\lambda_{\rm E}$. boundary between Pop. A and B, signifying a possible $M_{\rm BH}$ underestimate due to low S/N (i.e. loss of line wings in the case of 3C 179) or perhaps to a pole-on orientation of the emitting regions (e.g. Wills & Browne 1986; Rokaki et al. 2003; Sulentic et al. 2003; Zamfir et al. 2008).

5.2 Correlations between profile and physical parameters

5.2.1 M_{BH} *correlations*

Figs 12 and 13 show profile parameters, as AI and centroids, as a function of $M_{\rm BH}$, for Hβ and MgII, respectively, including our eRk quasars and the comparison samples. The immediate result is that there is no strong, clear correlation with $M_{\rm BH}$ – although an intriguing trend appears for the joint comparison sample. This is also supported

Table 9. Physical parameters measurement from the FP (BC + VBC) and BC of Hβ and MgII lines.

Object	Measurements from FP (BC + VBC)						Measurement from broad component only (BC)			
	Accretion parameters (Hβ)			Accretion parameters (MgII)			Accretion parameters (Hβ)		Accretion parameters (MgII)	
	$\log L_{\rm bol,\,5100}$	$\log M^a_{BH}$	$\log\lambda_{\rm E}{}^a$	$\log L_{\rm bol,\,3000}$	$\log M^b_{BH}$	$\log\lambda_{\rm E}{}^b$	$\log M^a_{BH}$	$\log\lambda_{\rm E}{}^a$	$\log M^b_{BH}$	$\log\lambda_{\rm E}{}^b$
(1)	(2)	(3)	(4)	(5)	(6)	(7)	(8)	(9)	(10)	(11)
PHL923	45.78	8.56	−0.90	45.80	8.58	−0.89	8.39	−0.73	8.43	−0.74
B2 0110 + 29	45.15	8.49	−1.45	44.98	8.26	−1.40	8.21	−1.18	8.15	−1.29
3C37	45.73	8.73	−1.11	45.66	8.76	−1.21	8.60	−0.98	8.64	−1.10
PKS 0230–051	46.11	8.89	−0.90	46.10	8.90	−0.92	8.66	−0.66	8.75	−0.77
3C94	46.57	9.25	−0.74	46.53	9.33	−0.92	9.35	−0.70	9.33	−0.73
PKS 0420–01	46.49	8.94	−0.57	46.17	8.77	−0.71	8.83	−0.45	8.62	−0.56
3C179	45.95	8.49	−0.64	45.86	8.71	−0.96	8.22	−0.38	8.54	−0.79
3C380	46.33	9.13	−0.92	46.18	8.99	−0.93	8.82	−0.60	8.80	−0.73
S5 1856 + 73	46.11	8.99	−1.00	45.93	8.99	−1.18	8.92	−0.93	8.84	−1.03
PKS 2208–137	45.86	8.49	−0.75	45.83	8.69	−0.97	8.43	−0.69	8.56	−0.84
PKS 2344 + 09	46.55	8.99	−0.55	46.49	9.16	−0.78	8.87	−0.44	9.01	−0.64

[a]Estimated from Vestergaard & Peterson (2006). [b]Estimated from Trakhtenbrot & Netzer (2012). Columns 2 and 5 in ergs s^{-1}. $M_{\rm BH}$ Columns in units of $M_\odot$.

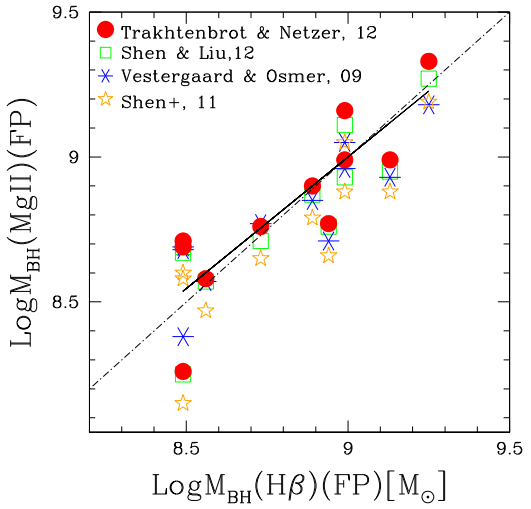

Figure 11. $M_{\rm BH}$ comparison for estimates from Hβ and MgII, FP FWHM measurement using different scaling laws. The abscissa is $M_{\rm BH}$ estimated by using the formula from Vestergaard & Peterson (2006). In ordinate, we plot different $M_{\rm BH}$ estimates for MgII, from Vestergaard & Osmer (2009), Shen et al. (2011), Trakhtenbrot & Netzer (2012), and Shen & Liu (2012). The dot–dashed line represents the 1:1 line, and the solid one represents the correlation between the masses estimated by using Vestergaard & Peterson (2006) for Hβ and Trakhtenbrot & Netzer (2012) for MgII. The Pearson correlation coefficient between the two estimates is $r = 0.91$.

by previous statistical tests for low-z Pop. B sources (Zamfir et al. 2010).

Restricting the attention to Hβ, for the joint comparison sample and irrespective of whether the sources are Pop. A or B, below $\log M_{\rm BH} \sim 8.5[{\rm M}_\odot]$ RL sources show a weak median redshift for $c(\frac{1}{4}) \approx 280 \pm 270\,{\rm km\,s^{-1}}$, while RQs show no significant shift nor asymmetry (median $c(\frac{1}{4}) \approx -20 \pm 180\,{\rm km\,s^{-1}}$, $\mu_{1/2}{\rm AI} \approx 0.01 \pm 0.08$). Above $\log M_{\rm BH} \sim 8.5\,[{\rm M}_\odot]$, there is an increase in scatter in the values of the AI and centroids, and a predominance of shifts to the red appears, especially for RL sources ($\mu_{1/2}c(\frac{1}{4}) \approx 660 \pm 650\,{\rm km\,s^{-1}}$, $\mu_{1/2}{\rm AI} \approx 0.1 \pm 0.1$), while RQs remain more symmetric (median $c(\frac{1}{4}) \approx 150 \pm 490\,{\rm km\,s^{-1}}$, AI $\approx 0.04 \pm 0.10$), albeit with a slight net shift to the red. Restricting now the attention to only Pop. B sources, Hβ yields similar results: RL show a trend towards the red with a median $c(\frac{1}{4}) \approx 300 \pm 270\,{\rm km\,s^{-1}}$ for $\log M_{\rm BH} \lesssim 8.5\,[{\rm M}_\odot]$, while the RQ counterpart a median centroid consistent with no shift ($c(\frac{1}{4}) \approx 30 \pm 280\,{\rm km\,s^{-1}}$). For the higher $M_{\rm BH}$ range, both RQ and RL Pop. B sources show a net shift to the red that reaches a median $c(\frac{1}{4}) \approx 680\,{\rm km\,s^{-1}}$ for the RL subsample. Consistently, for the whole comparison sample, the ratio of the number of sources with negative and positive $c(\frac{1}{4})$ is ≈ 1.2 for RQ for $\log M_{\rm BH} < 8.5$ and 0.61 for $\log M_{\rm BH} > 8.5$. The same ratio for RL sources is 0.45 and 0.31 for the two mass ranges, showing a net predominance of redshift. If the attention is restricted to Pop. B, we see a net predominance of redshifts for both RQ and RL in the higher mass range (ratio negative-to-positive $c(\frac{1}{4})$ is 0.38 and 0.30, respectively). In the lower $M_{\rm BH}$ range, the prevalence of redshifts is higher for RL (ratio ≈ 0.54) than for RQ (ratio ≈ 0.95) for which the distribution is fairly symmetric, as expected also by the almost zero median shift amplitude of $c(\frac{1}{4})$.

The intrinsic shift to red might be associated with gravitational redshift (e.g. Bon et al. 2015; Punsly et al. 2020) or with infall plus obscuration (Wang et al. 2017). However, the origin of the redward asymmetry is still unclear and the subject of ongoing investigations. Infall of gas towards the centre is an alternative to gravitational redshift that may also produce significant shifts to the red expected to grow in amplitude towards the line base (Netzer 1977; Penston et al. 1990; Fromerth & Melia 2001; Wang et al. 2017).

Related to MgII, Fig. 13 shows the centroid shift at the two different fractional intensities of the MgII line as a function of $M_{\rm BH}$ computed from FWHM MgII$_{\rm FP}$. The values of $c(\frac{1}{2})$ and $c(\frac{1}{4})$ are comparable, with a slight systematic difference of about 100 km s^{-1}. Considering the comparison composite samples from Marziani et al. (2013), Pop. B MgII centroid shifts close to the line base exceed the ones at the center by a modest amount of 200–300 km s^{-1}, at variance with Hβ: the Hβ line base is significantly more redshifted than the centre. For instance, the eRk sample sources show an average $c(\frac{1}{4})$–$c(\frac{1}{2}) \approx 800\,{\rm km\,s^{-1}}$. As mentioned above, the MgII profile retains a higher degree of symmetry than Hβ because of a less prominent VBC. Whatever the cause of the reward asymmetry might be, the MgII profile is apparently less affected than Hβ.

5.2.2 λ_E correlations

Several authors suggested that outflows are apparently more related to $\lambda_{\rm E}$ than to luminosity or $M_{\rm BH}$ (e.g. Abramowicz & Straub 2014;

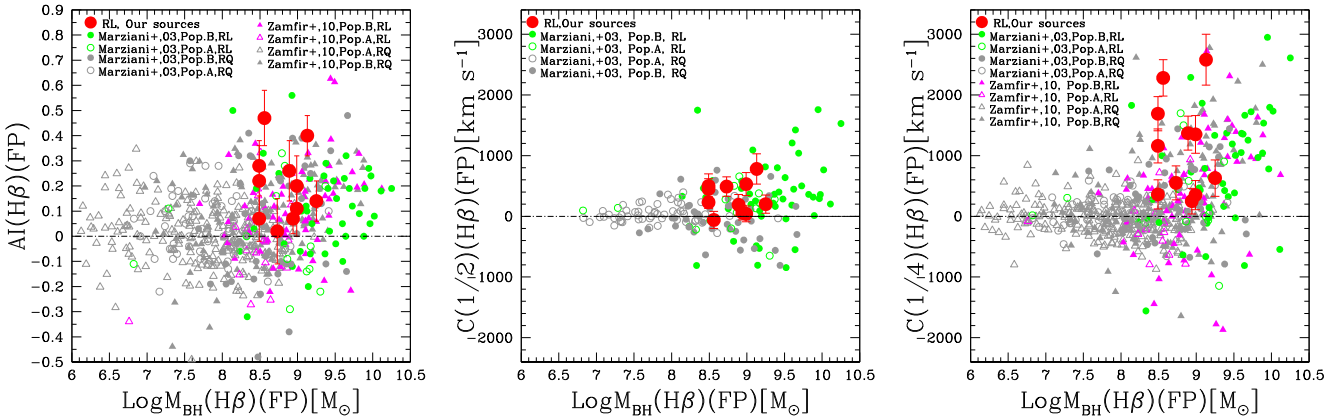

Figure 12. $M_{\rm BH}$ effect on line profile parameters, AI (left), on c($\frac{1}{2}$) and c($\frac{1}{4}$) (middle and right plots, respectively). Comparison samples were taken from Marziani et al. (2003a) for c($\frac{1}{2}$) and Marziani et al. (2003a) and Zamfir et al. (2010) for AI and c($\frac{1}{4}$). The large red solid circles represent the results from our RL spectra. The horizontal dot–dashed lines trace the symmetry line for zero AI, c($\frac{1}{2}$) and c($\frac{1}{4}$).

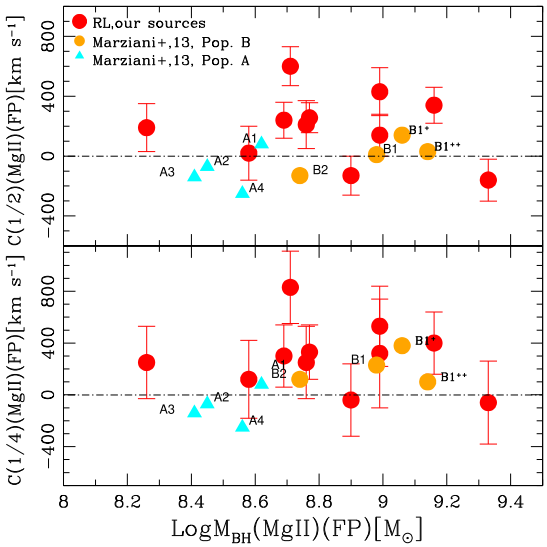

Figure 13. $M_{\rm BH}$ of MgII$_{\rm FP}$ and centroid shift comparison at c($\frac{1}{2}$) (upper) and at c($\frac{1}{4}$) (lower) of MgII. The large red solid circles represent the results from our RL spectra. A comparison sample was taken from the composite spectra of Marziani et al. (2013) and the meaning of symbols is as for Fig. 7.

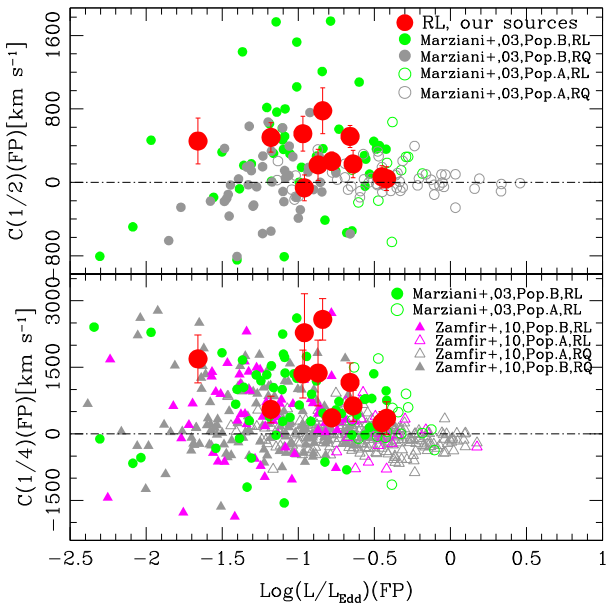

Figure 14. Dependence of Hβ c($\frac{1}{2}$) (upper) and c($\frac{1}{4}$) (lower) on log$\lambda_{\rm E}$ calculated from the FP. Comparison samples were taken from Marziani et al. (2003a) for c($\frac{1}{2}$) and Marziani et al. (2003a) and Zamfir et al. (2010) for c($\frac{1}{4}$)..

Sulentic et al. 2017). How c($\frac{1}{2}$), c($\frac{1}{4}$), and $\lambda_{\rm E}$ are related, in our eRk quasars and the comparison samples, is shown in Fig. 14.

Pop. B RL and RQ quasars belonging to the comparison samples are redshifted, and they generally possess low $\lambda_{\rm E}$. If the shift to the red is gravitational in origin, the line might be emitted from a region closer to the central SMBH, which results in larger shifts if the $\lambda_{\rm E}$ is lower. As there is a general consensus that outflows produce blueshifts (Marziani & Sulentic 2012a), the lower shifts at higher $\lambda_{\rm E}$ may be due to the increased relevance of radiation forces with respect to gravitation, which may push outward the emitting gas if there is a sort of radiation pressure/gravitation balance (Mathews 1993; Marconi et al. 2009; Netzer & Marziani 2010; Khajenabi 2015). Therefore, a difference between RL and RQ might be due to a combination of inflows and outflows that may result in a net slightly redshifted profile for RQ where winds are stronger (e.g. Bachev et al. 2004; Sulentic et al. 2007; Richards et al. 2011), and more redshift profiles for RLs, due to less prominent outflows.

5.3 Similarities and differences between RL and RQ quasars

For better visualization of the trends using the main comparison samples as well as the eRk sources, we analysed the distribution of the velocity centroids at 1/4 based on their population as well as radio type. In addition, we showed the median measurements of the comparison samples in equally spaced bins by using the semi-interquartile range as an estimate of the sample dispersion. Our eRk quasars are strong radio emitters with $\log R_{\rm K} > 3$ and very powerful with $\log P_{\nu} > 33.3$ [ergs s^{-1} Hz^{-1}] and include some of the highest $\log R_{\rm K}$ values ever observed. Objects with $\log R_{\rm K} \geq 3$ are most likely highly beamed, but they are still expected to be very powerful radio sources as suggested previously by Cohen et al. (2007).

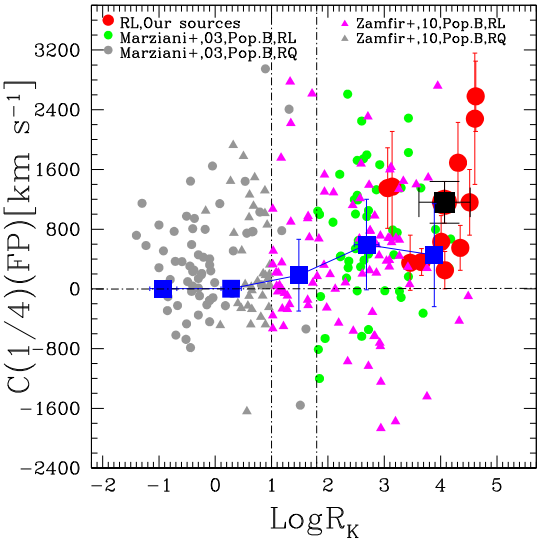

Figure 15. Relation between c($\frac{1}{4}$) of Hβ and radio-loudness parameter. Sources from Marziani et al. (2003a) and Zamfir et al. (2010) were taken as comparison sample. The connected blue solid squares represent the median value of the comparison sample distribution in equally-spaced bins where the vertical bars were computed by using the semi-interquartile range as an estimate of the sample dispersion. The horizontal bins denote, for each bin, the mid-point of the bin interval. The black solid square is the median value for our eRk quasars. The horizontal dot–dashed line traces the symmetric line in c($\frac{1}{4}$). The vertical lines at 1 and 1.8 mark the nominal RQ-RI and RI-RL boundaries (Zamfir et al. 2008).

A first result of the inter-comparison between RL and RQ sources is their distribution in the optical plane of the MS (see Fig. 4). In that figure, all of the eRk sources show a restricted domain occupation (mostly B1) compared to the RQ majority (taken from Zamfir et al. (2010). RQ sources are found in both Pop. A and Pop. B and are distributed along the MS in all bins. The RLs, with CD and FR II morphology, show a distribution centred in the region of low $R_{\rm FeII,\ opt}$ and broader FWHM. A restricted domain space occupation of Pop. B RL sources is also shown in the previous studies of Sulentic et al. (2000a); Sulentic et al. (2003). Similar considerations apply to the sources that are used to make the composite in Marziani et al. (2013, see their table 1 for the number of sources in different bins).

Fig. 15 relates the velocity centroid shift, c($\frac{1}{4}$) of Hβ to the radio loudness parameter, $R_{\rm K}$, for our eRk, and the Marziani et al. (2003a) and Zamfir et al. (2010) Pop. B sub-samples, represented in equally spaced bins of $R_{\rm K}$ (see also figure in Appendix B of the online supplementary material for the relation with c($\frac{1}{2}$)). The second result is that the Pop. B RL source distribution does not show a clear trend with the $R_{\rm K}$. However, there is a significant increase in the centroid shift between Pop. B RQ and Pop. B RL: the median c($\frac{1}{4}$) is $\approx$ 233 and 144 km s^{-1} for Pop. B RQ, and becomes $\approx$ 720 km s^{-1} and 440 km s^{-1} for the RL sources of Marziani et al. (2003a) and Zamfir et al. (2010) samples, respectively. The centroid shift for the eRk sources even reaches 1350 km s^{-1}. The significance of this difference needs to be further investigated in samples with matching $\lambda_{\rm E}$ and $M_{\rm BH}$ distributions, as systematic differences between RL and RQ sources are also found in terms of $M_{\rm BH}$. Considering the two comparison samples from Marziani et al. (2003a) and Zamfir et al. (2010) and our eRk, and then subdividing the Pop. B quasars only into RLs and RQs, the RQ sources have $\mu_{\frac{1}{2}}\log M_{\rm BH} \approx 8.18 \pm 0.53$ [M$_\odot$] and the RL's, $\mu_{\frac{1}{2}}\log M_{\rm BH} \approx 8.98 \pm 0.54$ [M$_\odot$], a 0.8 dex difference. In addition, considering the $\lambda_{\rm E}$, the RQs may be slightly higher accretors compared to the RLs, $\mu_{\frac{1}{2}}\log\lambda_{\rm E} \approx -1.081 \pm 0.156$ and $\mu_{\frac{1}{2}}\log\lambda_{\rm E} \approx -1.121 \pm 0.224$, respectively that become $\mu_{\frac{1}{2}}\log\lambda_{\rm E} \approx -0.785 \pm 0.343$ and $\mu_{\frac{1}{2}}\log\lambda_{\rm E} \approx -1.009 \pm 0.348$ with a difference of –0.224 dex if a constant optical bolometric correction of 10 is applied. Systematically lower $\lambda_{\rm E}$ and larger $M_{\rm BH}$ for Pop. B RL sources have been also found in several past works (e.g. Boroson 2002; Dunlop et al. 2003; McLure & Dunlop 2004).

Therefore, it is not necessarily appropriate to correlate radio loudness to a single variable such as c($\frac{1}{4}$), since other parameters such as $\lambda_{\rm E}$ and $M_{\rm BH}$ are expected to play a role (Woo & Urry 2002; Körding, Jester & Fender 2006). We need to take this into account if we compare the radio parameters and centroid shifts: the distribution of shifts appears to be slightly dependent on $M_{\rm BH}$, i.e. largest c($\frac{1}{4}$) values occur for the highest $M_{\rm BH}$ (Fig. 12) and lowest $\lambda_{\rm E}$ (Fig. 14). To verify whether there is a genuine effect of radio loudness on the c($\frac{1}{4}$), we considered the samples of Zamfir et al. (2010), and of Marziani et al. (2003a), added the 11 RLs of the present work and separated RQ and RL within Pop. B only, where most RL reside. This gave us 169 RQ and 145 RL Pop. B sources, of which 53 are eRk with $\log R_{\rm K} \geq 3$. The c($\frac{1}{4}$) distributions remain different ($P \sim 3 \times 10^{-5}$), suggesting that the shift amplitudes are higher in RL than in RQ. However, the $M_{\rm BH}$ distributions of RQ and RL are also markedly different ($P \sim 1 \times 10^{-4}$ that they are drawn from the same parent populations), with medians differing by $\delta\log M_{\rm BH} \approx 0.35$, while the two $\lambda_{\rm E}$ distributions are similar (Fig. 16).

Bootstrap replications of the RQ Pop. B samples were computed considering only distributions of $M_{\rm BH}$ and $\lambda_{\rm E}$ that were consistent with the ones of RL Pop. B (Fig. 16 upper right panel). Of the 1000 bootstrap distributions for the RQ Pop. B c($\frac{1}{4}$) $\lesssim$ 85 per cent were different from the RL one by a confidence level more than 2σ. Therefore, within the limitations of our sample, we are unable to detect a highly significant effect of radio loudness on the c($\frac{1}{4}$) shift amplitude. The majority of the RQ Pop. B bootstrapped distributions of c($\frac{1}{4}$) are largely overlapping with the RL one. The analysis thus confirms the statement of Marziani et al. (2003b) that the RQ and RL show similar velocity shift amplitudes, with the most extreme values (the ones attracting more attention) occurring for RLs.

Extreme RL sources, i.e. the 53 Pop. B sources with $\log R_{\rm K} \geq 3$, have a larger c($\frac{1}{4}$) shift with respect to the full population of RL, with distributions that are different at an even higher significance ($P \sim 10^{-6}$). We repeat the bootstrap analysis matching the RQ $M_{\rm BH}$ and $\lambda_{\rm E}$ distributions to the ones of the extreme RLs, and in this case, the difference at a 2σ confidence level is highly significant: less than 1 out of 1000 RQ c($\frac{1}{4}$) resampled distributions are statistically indistinguishable from the extreme RL one. The extreme RL sources also show c($\frac{1}{4}$) in excess with respect to the RL sources with $1.8 \leq \log R_{\rm K} < 3$, and the 2σ excess is still confirmed at a high confidence level. Therefore, the significance of the difference between RQ and RL sources is strongly dependent on sample biases, as it is mainly driven by the fraction of sources with high Kellermann ratio.

Equally important is not to forget the similarity between RQ and RL Pop. B sources. The same line profile phenomenology is observed in both classes, provided that a restriction to Pop. B is done for RQ quasars: RLs appear more extreme but with a large overlap in the line profile parameter distribution with RQs. This indicates that there could be only a quantitative effect on the BLR associated with the jet, without inducing any strong structural or dynamical change. Investigations that are beyond the scope of the present paper are needed to ascertain the physical origins of the excess c($\frac{1}{4}$) shift in the most powerful RL.

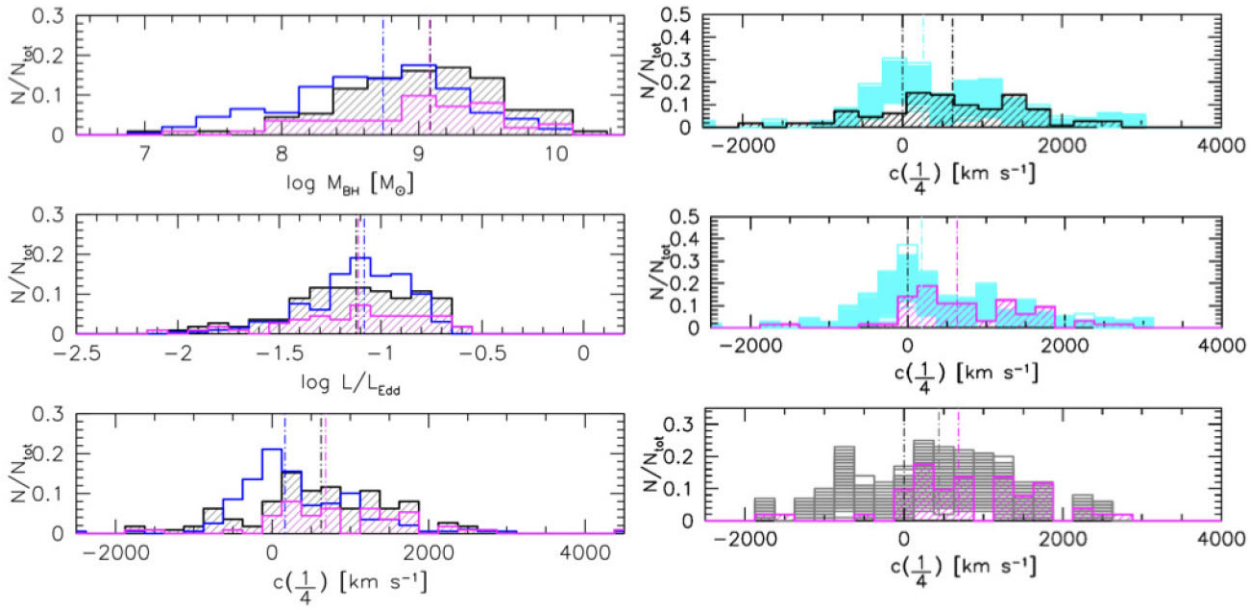

Figure 16. Results of the bootstrap analysis. Left-hand panels, from top to bottom: distributions of $M_{\rm BH}$, $L_{\rm bol}/L_{\rm Edd}$, and Hβ c($\frac{1}{4}$) for the RQ (blue), RL (black shaded), and extreme RL (log $R_{\rm K}\geq$3, magenta). Right-hand panels: comparison between Hβ c($\frac{1}{4}$) resampled distributions matching $M_{\rm BH}$ and $\lambda_{\rm E}$ and original distributions. Top: RL versus RQ bootstrap replications; middle: extreme RL versus RQ bootstrap; bottom: extreme RL versus rest of RL, i.e. objects with 1.8 $\leq$ log $R_{\rm K}$ <3. Vertical dot–dashed lines indicate medians.

6 CONCLUSIONS

This work presented new long-slit simultaneous near-UV and optical spectra of 11 relativistically jetted quasars selected on the basis of their extreme radio emission (log $R_{\rm K} > 3$, the eRk sources) with redshifts 0.35 $\lesssim$ z $\lesssim$ 1, and studied their spectroscopic properties by using the optical projection of the 4DE1 parameter space, i.e. the so-called quasar MS. Our analysis focused mainly on the spectral fitting of the strongest emission lines recorded on our spectra, MgII, and Hβ, by using `specfit` routine within the `IRAF` package. We aimed to quantify broad emission line differences between RL and RQ quasars, paying special attention to the quasars with extreme radio emission.

The main findings that we draw from this study are:

(i) The eRk quasars presented in this paper occupy a much more restricted domain in the optical plane (∼bin B1) compared to the RQ sources of the comparison samples. This confirms the result of Zamfir et al. (2008) who found that powerful jetted sources tend to occupy mainly the Pop. B region of the MS.

(ii) The UV plane formed from FWHM of MgII and FeII$_{\rm UV}$ looks similar to the optical plane. As in the optical plane, our quasars occupy a more restricted domain than the full quasar population, with low $R_{\rm FeII,\,UV}$. There is no correlation between the EW of FeII$_{\rm UV}$ and FeII$_{\rm opt}$ in our eRk sample.

(iii) The FWHM of MgII is systematically narrower than FWHM Hβ by about 10 per cent. This holds for both the full profile (BC + VBC) and if only the broad component is considered for our eRk sample, a result consistent with previous studies.

(iv) Both Hβ and MgII lines show profile shifts and asymmetries towards the red. The centroid shift of the line base c($\frac{1}{4}$), as well as the asymmetry index, are larger in Hβ than MgII.

(v) Hβ and MgII appear to be provide consistent virial $M_{\rm BH}$ estimates. The eRk quasars of this paper lie within the range of log$M_{\rm BH}$ = 8.49–9.25[M$_\odot$] and 8.26–9.33[M$_\odot$] when using H$\beta_{\rm FP}$ and MgII$_{\rm FP}$, respectively. The resulting log$\lambda_{\rm E}$ has a range of [−1.65, −0.42] and [−1.40, −0.71].

(vi) Joining the sources studied in this work with comparison samples, we find that the distribution of shifts appears to be slightly dependent on $M_{\rm BH}$ in which larger c($\frac{1}{4}$) values occur for the highest $M_{\rm BH}$ and lowest $\lambda_{\rm E}$ values. A possible explanation is offered by a combination of outflow and infall (or gravitational redshift) contributing to blueshifted and redshifted excesses, respectively, with the outflow component being minimal in the RL Hβ and MgII profiles.

(vii) There is a trend between the velocity shifts, stronger for c($\frac{1}{4}$), and $R_{\rm K}$: Pop. B RL quasars tend to have larger velocity shifts to the red than RQs. The difference is found to be only marginally significant if the RQ and RL $M_{\rm BH}$ and $\lambda_{\rm E}$ distributions are matched. However, the difference becomes highly significant if the comparison is carried between eRk and RQ Pop. B AGN.

There is apparently no evidence of outflow in the broad-line profiles of our eRk sources. The only evidence is provided by a slight asymmetry of [O III]. Further observations of HILs such as CIVλ1549 would be needed to assess the extent of any mildly ionized outflow origination from the accretion disc.

ACKNOWLEDGEMENTS

The authors thank the anonymous referees for their valuable suggestions that helped us to significantly improve the paper. STM acknowledges the support from Jimma University under the Ministry of Science and Higher Education. STM and MP acknowledge financial support from the Space Science and Geospatial Institute (SSGI) under the Ethiopian Ministry of Innovation and Technology (MInT). STM, ADO, and MP acknowledge financial support through the grant CSIC I-COOP + 2020, COOPA20447. STM especially acknowledges the IAA for all the support received during the two stays. ADO, MP, JP, PM, and IM acknowledge financial support

from the Spanish Ministerio de Ciencia e Innovación–Agencia Estatal de Investigación through projects PID2019-106027GB-C41 and PID2019–106027GB–C43, and from the Severo Ochoa grants SEV-2017-0709 and CEX2021-001131-S funded by MCIN/AEI/ 10.13039/501100011033. MAMC has been supported by the Spanish Research project PID 2021–122961NB-IOO.

DATA AVAILABILITY

This work used original data observed by the group using the Cassegrain TWIN spectrograph of the 3.5 m telescope at the CAHA (Almer´ıa, Spain)[7] and present new optical and near-UV spectra of 11 powerful jetted quasars. In support of this study, the additional data used in this article were obtained from the public sources cited in the article (or references therein).

REFERENCES

Abramowicz M. A., Straub O., 2014, Scholarpedia, 9, 2408
Antonucci R., 1993, ARA&A, 31, 473
Antonucci R., 2012, Astron. Astrophys. Trans., 27, 557
Bañados E. et al., 2018, Nature, 553, 473
Bachev R., Marziani P., Sulentic J. W., Zamanov R., Calvani M., Dultzin-Hacyan D., 2004, ApJ, 617, 171
Bao D.-W. et al., 2022, ApJS, 262, 14
Barth A. J. et al., 2013, ApJ, 769, 128
Becker R. H., White R. L., Helfand D. J., 1995, ApJ, 450, 559
Blandford R., Meier D., Readhead A., 2019, ARA&A, 57, 467
Blundell K. M., Beasley A. J., Bicknell G. V., 2003, ApJ, 591, L103
Bon N., Bon E., Marziani P., Jovanović P., 2015, Ap&SS, 360, 7
Bon N., Marziani P., Bon E., Negrete C. A., Dultzin D., del Olmo A., D'Onofrio M., Martínez-Aldama M. L., 2020, A&A, 635, A151
Boroson T. A., 2002, ApJ, 565, 78
Boroson T. A., Green R. F., 1992, ApJS, 80, 109
Bruhweiler F., Verner E., 2008, ApJ, 675, 83
Buttiglione S., Capetti A., Celotti A., Axon D. J., Chiaberge M., Macchetto F. D., Sparks W. B., 2010, A&A, 509, A6
Calderone G., Nicastro L., Ghisellini G., Dotti M., Sbarrato T., Shankar F., Colpi M., 2017, MNRAS, 472, 4051
Chakraborty A., Bhattacharjee A., Brotherton M. S., Chatterjee R., Chatterjee S., Gilbert M., 2022, MNRAS, 516, 2824
Cirasuolo M., Magliocchetti M., Celotti A., Danese L., 2003, MNRAS, 341, 993
Cohen M. H., Lister M. L., Homan D. C., Kadler M., Kellermann K. I., Kovalev Y. Y., Vermeulen R. C., 2007, ApJ, 658, 232
Collin-Souffrin S., Dyson J. E., McDowell J. C., Perry J. J., 1988, MNRAS, 232, 539
Collin S., Kawaguchi T., Peterson B. M., Vestergaard M., 2006, A&A, 456, 75
Condon J. J., Cotton W. D., Greisen E. W., Yin Q. F., Perley R. A., Taylor G. B., Broderick J. J., 1998, AJ, 115, 1693
Corbin M. R., 1997, ApJS, 113, 245
Coziol R., Andernach H., Torres-Papaqui J. P., Ortega-Minakata R. A., Moreno del Rio F., 2017, MNRAS, 466, 921
Davis S. W., Tchekhovskoy A., 2020, ARA&A, 58, 407
Deconto-Machado A., del Olmo A., Marziani P., Perea J., Stirpe G., 2022, Astron. Nachr., 343, e210084
Dimitrijević M. S., Popović L. Č., Kovačević J., Dačić M., Ilić D., 2007, MNRAS, 374, 1181
Dunlop J. S., McLure R. J., Kukula M. J., Baum S. A., O'Dea C. P., Hughes D. H., 2003, MNRAS, 340, 1095
Fraix-Burnet D., Marziani P., D'Onofrio M., Dultzin D., 2017, Front. Astron. Space Sci., 4, 1
Fromerth M. J., Melia F., 2001, ApJ, 549, 205
Gallimore J. F., Axon D. J., O'Dea C. P., Baum S. A., Pedlar A., 2006, AJ, 132, 546
Ganci V., Marziani P., D'Onofrio M., del Olmo A., Bon E., Bon N., Negrete C. A., 2019, A&A, 630, A110
Gaskell C. M., 1982, Lick Obs. Bull., 927, 1
Gaskell C. M., Anderson F. C., Birmingham S. Á., Ghosh S., 2022, preprint (arXiv:2208.11437)
Giustini M., Proga D., 2019, A&A, 630, A94
Gürkan G. et al., 2015, MNRAS, 452, 3776
Hao H. et al., 2014, preprint (arXiv:1408.1090)
Hartley P., Jackson N., Sluse D., Stacey H. R., Vives-Arias H., 2019, MNRAS, 485, 3009
Hernitschek N., Schlafly E. F., Sesar B., Rix H. W., Hogg D. W., Ivezic Z., Grebel E. K., 2016, CoKon, 105, 85
Ho L. C., 2008, ARA&A, 46, 475
Ho L. C., Kim M., 2015, ApJ, 809, 123
Jin C., Done C., Ward M., 2017, MNRAS, 468, 3663
Kaspi S., Smith P. S., Netzer H., Maoz D., Jannuzi B. T., Giveon U., 2000, ApJ, 533, 631
Kellermann K. I., Sramek R., Schmidt M., Shaffer D. B., Green R., 1989, AJ, 98, 1195
Kellermann K. I., Condon J. J., Kimball A. E., Perley R. A., Ivezić Ž., 2016, ApJ, 831, 168
Khajenabi F., 2015, MNRAS, 446, 1848
Komossa S., Xu D., Zhou H., Storchi-Bergmann T., Binette L., 2008, ApJ, 680, 926
Körding E. G., Jester S., Fender R., 2006, MNRAS, 372, 1366
Kovačević-Dojčinović J., Popović L. Č., 2015, ApJS, 221, 35
Kovačević-Dojčinović J., Marčeta-Mandić S., Popović L. Č., 2017, Front. Astron. Space Sci., 4, 7
Kovačević-Dojčinović J., Dojčinović I., Lakićević M., Popović L. Č., 2022, A&A, 659, A130
Kovačević J., Popović L. Č., Dimitrijević M. S., 2010, ApJS, 189, 15
Kovačević J., Popović L. Č., Kollatschny W., 2014, Adv. Space Res., 54, 1347
Kriss G., 1994, in Crabtree D. R., Hanisch R. J., Barnes J., eds, ASP Conf. Ser. Vol. 61, Astronomical Data Analysis Software and Systems III. Astron. Soc. Pac., San Francisco, p. 437
Kuźmicz A., Sethi S., Jamrozy M., 2021, ApJ, 922, 52
Lagos C. D. P., Padilla N. D., Cora S. A., 2009, MNRAS, 395, 625
Lapi A., Shankar F., Mao J., Granato G. L., Silva L., De Zotti G., Danese L., 2006, ApJ, 650, 42
Levenberg K., 1944, QApMa, 2, 164
Malkan M. A., Oke J. B., 1983, ApJ, 265, 92
Marconi A., Hunt L. K., 2003, ApJ, 589, L21
Marconi A., Axon D. J., Maiolino R., Nagao T., Pietrini P., Risaliti G., Robinson A., Torricelli G., 2009, ApJ, 698, L103
Marinello M., Rodríguez-Ardila A., Marziani P., Sigut A., Pradhan A., 2020, MNRAS, 494, 4187
Martínez-Aldama M. L., Dultzin D., Marziani P., Sulentic J. W., Bressan A., Chen Y., Stirpe G. M., 2015, ApJS, 217, 3
Marziani P., Sulentic J. W., 2012a, A&AR, 7, 33
Marziani P., Sulentic J. W., 2012b, New Astron. Rev., 56, 49
Marziani P., Sulentic J. W., Zwitter T., Dultzin-Hacyan D., Calvani M., 2001, ApJ, 558, 553
Marziani P., Sulentic J. W., Zamanov R., Calvani M., Dultzin-Hacyan D., Bachev R., Zwitter T., 2003a, ApJS, 145, 199
Marziani P., Zamanov R. K., Sulentic J. W., Calvani M., 2003b, MNRAS, 345, 1133
Marziani P., Sulentic J. W., Stirpe G. M., Zamfir S., Calvani M., 2009, A&A, 495, 83
Marziani P., Sulentic J. W., Negrete C. A., Dultzin D., Zamfir S., Bachev R., 2010, MNRAS, 409, 1033
Marziani P., Sulentic J. W., Plauchu-Frayn I., del Olmo A., 2013, A&A, 555, A89
Marziani P., Sulentic J. W., Stirpe G. M., Dultzin D., Del Olmo A., Martínez-Carballo M. A., 2016, Ap&SS, 361, 3
Marziani P. et al., 2018, Front. Astron. Space Sci., 5, 6

[7] http://www.caha.es/

Marziani P., Berton M., Panda S., Bon E., 2021, Universe, 7, 484
Marziani P., Panda S., Deconto Machado A., Del Olmo A., 2023, Galaxies, 11, 52
Mathews W. G., 1993, ApJ, 412, L17
Mathews W. G., Ferland G. J., 1987, ApJ, 323, 456
Mathur S., Kuraszkiewicz J., Czerny B., 2001, New Astron., 6, 321
McLure R. J., Dunlop J. S., 2004, in Mújica R., Maiolino R., eds, Multiwavelength AGN Surveys. p. 389
McLure R. J., Jarvis M. J., 2002, MNRAS, 337, 109
McLure R. J., Jarvis M. J., Targett T. A., Dunlop J. S., Best P. N., 2006, New Astron. Rev., 50, 782
Middelberg E. et al., 2004, A&A, 417, 925
Netzer H., 1977, MNRAS, 181, 89
Netzer H., 2015, ARA&A, 53, 365
Netzer H., 2019, MNRAS, 488, 5185
Netzer H., Marziani P., 2010, ApJ, 724, 318
Osterbrock D. E., 1988, in Miller H. R., Wiita P. J., eds, Active Galactic Nuclei, Vol. 307. Springer-Verlag, Berlin, Heidelberg, New York, p. 1
Osterbrock D. E., Mathews W. G., 1986, ARA&A, 24, 171
Osterbrock D. E., Pogge R. W., 1985, ApJ, 297, 166
Padovani P. et al., 2017, A&AR, 25, 2
Panda S., Czerny B., Done C., Kubota A., 2019a, ApJ, 875, 133
Panda S., Marziani P., Czerny B., 2019b, ApJ, 882, 79
Panessa F., Baldi R. D., Laor A., Padovani P., Behar E., McHardy I., 2019, Nat. Astron., 3, 387
Penston M. V., Croft S., Basu D., Fuller N., 1990, MNRAS, 244, 357
Peterson B. M., 1997, An Introduction to Active Galactic Nuclei. Cambridge Univ. Press, Cambridge, New York
Peterson B. M., Wandel A., 1999, ApJ, 521, L95
Peterson B. M., Wandel A., 2000, ApJ, 540, L13
Plavin A. V., Kovalev Y. Y., Pushkarev A. B., 2022, ApJS, 260, 4
Popović L. Č., Kovačević J., 2011, ApJ, 738, 68
Popović L. Č., Smirnova A. A., Kovačević J., Moiseev A. V., Afanasiev V. L., 2009, AJ, 137, 3548
Popović L. Č., Kovačević-Dojčinović J., Marčeta-Mandić S., 2019, MNRAS, 484, 3180
Punsly B., Marziani P., Berton M., Kharb P., 2020, ApJ, 903, 44
Rakić N., 2022, MNRAS, 516, 1624
Rakić N., La Mura G., Ilić D., Shapovalova A. I., Kollatschny W., Rafanelli P., Popović L. Č., 2017, A&A, 603, A49
Rees M. J., 1984, ARA&A, 22, 471
Richards G. T. et al., 2011, AJ, 141, 167
Rokaki E., Lawrence A., Economou F., Mastichiadis A., 2003, MNRAS, 340, 1298
Sbarrato T., Ghisellini G., Giovannini G., Giroletti M., 2021, A&A, 655, A95
Shankar F., Dai X., Sivakoff G. R., 2008, ApJ, 687, 859
Shapovalova A. I. et al., 2012, ApJS, 202, 10
Shen Y., 2013, Bull. Astron. Soc. India, 41, 61
Shen Y., Ho L. C., 2014, Nature, 513, 210
Shen Y., Liu X., 2012, ApJ, 753, 125
Shen Y. et al., 2011, ApJS, 194, 45
Shields G. A., 1978, Nature, 272, 706
Sigut T. A. A., Pradhan A. K., 2003, ApJS, 145, 15
Sikora M., Stawarz Ł., Lasota J.-P., 2007, ApJ, 658, 815
Snedden S. A., Gaskell C. M., 2007, ApJ, 669, 126
Śniegowska M., Czerny B., You B., Panda S., Wang J. M., Hryniewicz K., Wildy C., 2018, A&A, 613, A38
Śniegowska M., Kozłowski S., Czerny B., Panda S., Hryniewicz K., 2020, ApJ, 900, 64
Śniegowska M., Marziani P., Czerny B., Panda S., Martínez-Aldama M. L., del Olmo A., D'Onofrio M., 2021, ApJ, 910, 115
Strateva I. V. et al., 2003, AJ, 126, 1720
Sulentic J. W., Marziani P., Dultzin-Hacyan D., 2000a, ARA&A, 38, 521
Sulentic J. W., Zwitter T., Marziani P., Dultzin-Hacyan D., 2000b, ApJ, 536, L5
Sulentic J. W., Marziani P., Zwitter T., Dultzin-Hacyan D., Calvani M., 2000c, ApJ, 545, L15
Sulentic J. W., Marziani P., Zamanov R., Bachev R., Calvani M., Dultzin-Hacyan D., 2002, ApJ, 566, L71
Sulentic J. W., Zamfir S., Marziani P., Bachev R., Calvani M., Dultzin-Hacyan D., 2003, ApJ, 597, L17
Sulentic J. W., Bachev R., Marziani P., Negrete C. A., Dultzin D., 2007, ApJ, 666, 757
Sulentic J., Marziani P., Zamfir S., 2011, Baltic Astron., 20, 427
Sulentic J. W., Marziani P., D'Onofrio M., 2012, in D'Onofrio M., Marziani P., Sulentic J. W., eds, Astrophysics and Space Science Library, Vol. 386, Fifty Years of Quasars: From Early Observations and Ideas to Future Research. p. 549
Sulentic J. W. et al., 2017, A&A, 608, A122
Tchekhovskoy A., McKinney J. C., Narayan R., 2009, ApJ, 699, 1789
Tody D., 1986, in Crawford D. L.ed., Proc. SPIE Conf. Ser. Vol. 627, Instrumentation in Astronomy VI. SPIE, Bellingham, p. 733
Trakhtenbrot B., Netzer H., 2012, MNRAS, 427, 3081
Ulvestad J. S., Roy A. L., Colbert E. J. M., Wilson A. S., 1998, ApJ, 496, 196
Ulvestad J. S., Antonucci R. R. J., Barvainis R., 2005, ApJ, 621, 123
Urry C. M., Padovani P., 1995, PASP, 107, 803
Vanden Berk D. E. et al., 2001, AJ, 122, 549
Véron-Cetty M. P., Véron P., 2010, A&A, 518, A10
Vestergaard M., Osmer P. S., 2009, ApJ, 699, 800
Vestergaard M., Peterson B. M., 2006, ApJ, 641, 689
Vietri G. et al., 2020, A&A, 644, A175
Vollmer B. et al., 2010, A&A, 511, A53
Wang J.-G. et al., 2009, ApJ, 707, 1334
Wang J.-M., Du P., Brotherton M. S., Hu C., Songsheng Y.-Y., Li Y.-R., Shi Y., Zhang Z.-X., 2017, Nature Astron., 1, 775
White R. L., Becker R. H., Helfand D. J., 2005, AJ, 130, 586
Wills B. J., Browne I. W. A., 1986, ApJ, 302, 56
Wolf J. et al., 2020, MNRAS, 492, 3580
Woo J.-H., Urry C. M., 2002, ApJ, 579, 530
Xu C., Livio M., Baum S., 1999, AJ, 118, 1169
Zamanov R., Marziani P., Sulentic J. W., Calvani M., Dultzin-Hacyan D., Bachev R., 2002, ApJ, 576, L9
Zamfir S., Sulentic J. W., Marziani P., 2008, MNRAS, 387, 856
Zamfir S., Sulentic J. W., Marziani P., Dultzin D., 2010, MNRAS, 403, 1759
Zhang K., Dong X.-B., Wang T.-G., Gaskell C. M., 2011, ApJ, 737, 71

SUPPORTING INFORMATION

Supplementary data are available at *MNRAS* online.

Figure S1 FIRST cut-out image in arcmin (**left**) and an overlay of FIRST cut-out image on the Optical Pan-STARRS image (**right**) of the source **PHL 923, (00 59 05.5148 + 00 06 51.621).**

Figure S2 NVSS contour map (**left**) and an overlay of NVSS contour map on the Optical Pan-STARRS image (**right**) of **B2 0110+29, (01 13 24.200 + 29 58 15.00)**

Figure S3 FIRST cut-out image obtained with maximum scaling to be 1000 mJy (**left**) and an overlay of FIRST cut-out image on the Optical Pan-STARRS image (**right**) for the source **3C 37, (01 18 18.489 + 02 58 05.97).**

Figure S4 FIRST cut-out image obtained with maximum scaling to be 1000 mJy to show the separate components (**left**) and an overlay of FIRST cut-out on the Optical Pan-STARRS image (**right**) for the source **PKS 0230-051, (02 33 22.18 − 04 55 06.8.)**

Figure S5 FIRST cut-out image obtained with maximum scaling to be 1000 mJy to show the separate components (**left**) and an overlay

of FIRST cut-out on the Optical Pan-STARRS image (**right**) for the source **3C 94, (03 52 30.552 − 07 11 02.32).**

Figure S6 NVSS contour map (**left**) and an overlay of NVSS contour map on the Optical Pan-STARRS image (**right**) of the source **PKS 2208-137, (22 11 24.0994 − 13 28 09.723).**

Figure S7 FIRST cut-out image obtained with maximum scaling to be 1000 mJy to show the separate components (**left**) and an overlay of FIRST cut-out on the Optical Pan-STARRS image (**right**) for the source **PKS 2344+09, (23 46 36.8385 + 09 30 45.515).**

Figure S8 Relation between Hβ c($\frac{1}{2}$) with the logarithm of radio loudness parameter that indicates the median distribution to show how the trend is with the comparison sample in which Pop.A and Pop.B are shown from Marziani et al. (2003a).